ELECTRON MICROSCOPE IMAGE CONTRAST OF SMALL DISLOCATION LOOPS AND STACKING-FAULT TETRAHEDRA

By D. K. SALDIN, A. Y. STATHOPOULOS and M. J. WHELAN, F.R.S.
Department of Metallurgy and Science of Materials, University of Oxford, Parks Road, Oxford OX1 3PH, U.K.

(*Received* 16 *November* 1978)

[Plates 1–8]

CONTENTS

PAGE

1. Introduction 524
2. The computer simulation system 525
   (*a*) The effect of tilting the foil 525
   (*b*) Other details 525
3. Experimental details 527
4. Results 527
   (*a*) Images of Frank loops 528
      (i) The effect of varying the operating reflexion **g** 528
         (*A*) The ⟨011⟩ orientation 528
         (*B*) 'Butterfly' images 529
         (*C*) The ⟨001⟩ orientation 529
      (ii) Depth dependence of images 530
      (iii) Loop size 531
      (iv) Dependence on deviation parameter 531
   (*b*) Images of stacking-fault tetrahedra 532
      (i) The ⟨011⟩ orientation 532
      (ii) The ⟨001⟩ orientation 533
   (*c*) Images of loops with non-edge character 533
5. Direction of black–white streaking 534
6. Discussion and conclusions 534

Appendix: Determinants of forms of black–white lobes 535

References 536

With the use of the method described in the preceding paper (to be referred to subsequently as I) for constructing the displacement fields, the electron microscope image contrast of small dislocation loops and of stacking-fault tetrahedra has been computed from numerical solutions of the Howie–Whelan (1961) equations. The computer-simulated images, displayed in the form of half-tone pictures, have been used to identify the nature and geometry of such defects in ion-irradiated foils. A systematic study of the contrast of small Frank loops in Cu^+ ion irradiated copper under a wide variety of diffraction conditions is reported. In particular the variations of the contrast of loops edge-on and inclined to the electron beam with the operating Bragg reflexion, the thickness and inclination of the foil, depth of the defect in the foil and deviation from the Bragg-reflecting condition have been studied. Methods of obtaining useful information, such as the diameters of the loops, are suggested. The contrast of stacking-fault tetrahedra, and of non-edge perfect dislocation loops in ion-irradiated molybdenum is also investigated.

1. Introduction

It has been known since the work of Essmann & Wilkens (1964) that small centres of strain such as point-defect clusters exhibit 'black–white' contrast when imaged under dynamical two-beam conditions in the electron microscope. Furthermore, if a vector $\boldsymbol{l}$ is defined as that joining the centre of the black lobe to the centre of the white lobe, it was found that this vector reversed direction in a periodic way as the depth of the defect in the foil was varied, giving rise to the so-called 'layer structure'. It was found that the sign of $\boldsymbol{g}\cdot\boldsymbol{l}$ in each layer (where $\boldsymbol{g}$ is the reciprocal lattice vector of the operating reflexion) depended on whether the centre of strain was of vacancy or of interstitial character. These and other observations (for reviews see Ruhle 1969; Wilkens 1970*a*, *b*) were elegantly explained by theories based on the kinematical scattering of Bloch waves (see, for example, Wilkens 1970*a*; Hirsch 1978). These theories considered only relatively weak inter-branch scattering and were therefore only accurate in the long-range parts of the strain field. They did not accurately predict the nature of the contrast in the region of the interface between the black and the white lobes. A more sophisticated theory has been developed by Katerbau (1976) which exactly calculates the magnitudes of the interbranch and intrabranch scattering, but, in order to make the expressions tractable, uses a very simple model for the strain field of edge-on dislocation loop, based on a double stacking fault. Nevertheless, this theory adequately explains most of the qualitative features of the contrast in the interface region. A more exact method of identifying the nature of small centres of strain is the comparison of electron micrographs with computer-simulated images. Such methods have been developed for dislocation loops by Bullough *et al.* (1971) and Maher *et al.* (1971). These authors studied mainly large resolvable loops. The work has been extended by Eyre *et al.* (1977*a*, *b*) to the case of small loops (i.e. with diameters, $d < \frac{1}{4}\xi_g$, where ξ_g is the two-beam extinction distance) of edge character, primarily in the b.c.c. metal molybdenum. In the present paper, the results are reported of a systematic study, under a wide variety of diffraction conditions, of the contrast of small Frank loops in copper and of stacking-fault tetrahedra. The electron micrographs shown of the latter defects are from a Cu 10 at. % Al alloy (whose stacking-fault energy is about 11 mJ m^{-2} (Carter & Ray 1977), the value for copper being about 41 mJ m^{-2} (Stobbs & Sworn 1971; Cockayne *et al.* 1971). Tetrahedra are more commonly found in low stacking-fault energy materials. Also discussed are the images of non-edge loops in molybdenum.

2. The computer simulation system

Beam intensities at a grid of points on the electron-exit surface of the foil were computed, using the column approximation (Hirsch *et al.* 1960). The Howie–Whelan (1961) equations of diffraction contrast were solved by computer in the two-beam case for the displacement field due to the defect. The numerical solution of the equations was performed by means of Gill's (1951) method. Relativistically corrected Smith & Burge (1962) values for the atomic scattering factor were employed to compute the extinction distances. The absorption parameters used were those given by Radi (1970).

(*a*) *The effect of tilting the foil*

The Howie–Whelan equations are only strictly valid in the symmetric Laue case where the Bragg planes are perpendicular to the foil surface. In transmission electron microscopy, however, it is quite common to tilt the specimen through large angles in order to make use of diffraction from lattice planes not perpendicular to the foil surface. It has been suggested by Head *et al.* (1973), and demonstrated more rigorously by Saldin *et al.* (1978*b*), that as long as the tilt of the foil from the plane perpendicular to the incident beam is not greater than about 70°, the Howie–Whelan equations may to a good approximation still be used to compute image contrast. If the columns are taken in the direction of the diffracted beam, the effect of the tilt is taken into account by adjusting the positions of the ends of each column to correspond with the entry and exit surfaces of the foil. Consider in figure 1 the orthogonal system of axes $\boldsymbol{x}$, $\boldsymbol{y}$, $\boldsymbol{z}$ which were referred to as $\boldsymbol{E}$, $\boldsymbol{F}$, $\boldsymbol{G}$ in I. The $\boldsymbol{z}$ axis points in the direction anti-parallel to the electron beam and the origin O lies on the entrance surface of the foil. The columns used in the calculation can then be chosen parallel to the $\boldsymbol{z}$ axis and their position can be specified by their intersections with the x–y plane. If $P(x, y)$ is the point of intersection of a column with this plane, it follows that the electron entry end T of the column will be displaced below the x–y plane by an amount

$$\Delta z = \frac{N_x x + N_y y}{\sqrt{(N_x^2 + N_y^2)}} \tan \alpha$$

where N_x and N_y are the resolved components of the foil normal vector $\boldsymbol{N}$ with respect to the $\boldsymbol{x}$ and $\boldsymbol{y}$ axes respectively and α is the angle between $\boldsymbol{N}$ and $\boldsymbol{z}$.

(*b*) *Other details*

An interpolation scheme similar to that described by Maher *et al.* (1971) was used to obtain a fairly fine spacing of picture points. The resulting grid of numbers proportional to the local electron intensities was converted into a (112 × 112) grid of 200 μm square dots plotted adjacently on a transparent photographic film, reproducing the intensity distribution on a (negative) electron micrograph. This was achieved by using an Optronics Photowrite image display system which is capable of plotting finely spaced dots at any of 64 different grey levels. The system was calibrated by using a microdensitometer to find the optical density of each of the grey levels, and by comparing the graph so obtained with a graph relating electron dose to optical density on electron microscope film obtained experimentally (Maher *et al.* 1971). Elimination of optical density between the two graphs enabled the association of an electron dose with each grey level. Electron micrographs are taken under a wide variety of different beam intensities and exposure times. If, as in the case of the black–white images considered here, features of image contrast both above and below background level are to be studied, it is usual to adjust the electron dose so as to

obtain a background intensity corresponding to an optical density of about unity on experimental micrographs. The calculated electron intensities were therefore normalized with respect to their background intensity and the graph of electron dose against grey level label was scaled so as to make a (normalized) electron dose of unity (i.e. background level) correspond to an optical

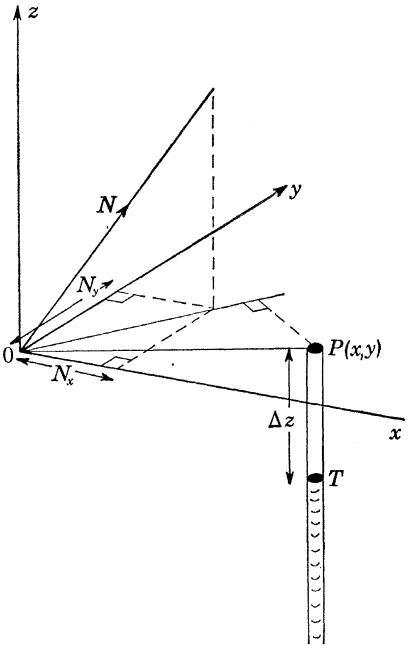

FIGURE 1. Specification of tilt of foil.

density of unity. This enables the association of the normalized electron intensities from the computer with the normalized electron dose scale and thus allows the appropriate grey level to be found.

From the half-tone negatives produced in this way, positive prints were made. In practice a slight defocusing of the printed image was found to be useful in blurring the dots to create the effect of continuous tone.

DESCRIPTION OF PLATE 1

FIGURE 2. Frank loops, $\boldsymbol{g} = (1\bar{1}1)$. Experimental image: $\boldsymbol{z} = [011]$, $\boldsymbol{N} \approx [023]$. Computed images: $\boldsymbol{z} = \boldsymbol{N} = [011]$, $t = 2\xi_g$, $(t-d) = \frac{1}{8}\xi_g$, edge length of computed images = 8.1 nm. Dark field.

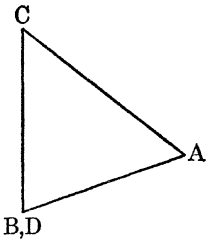

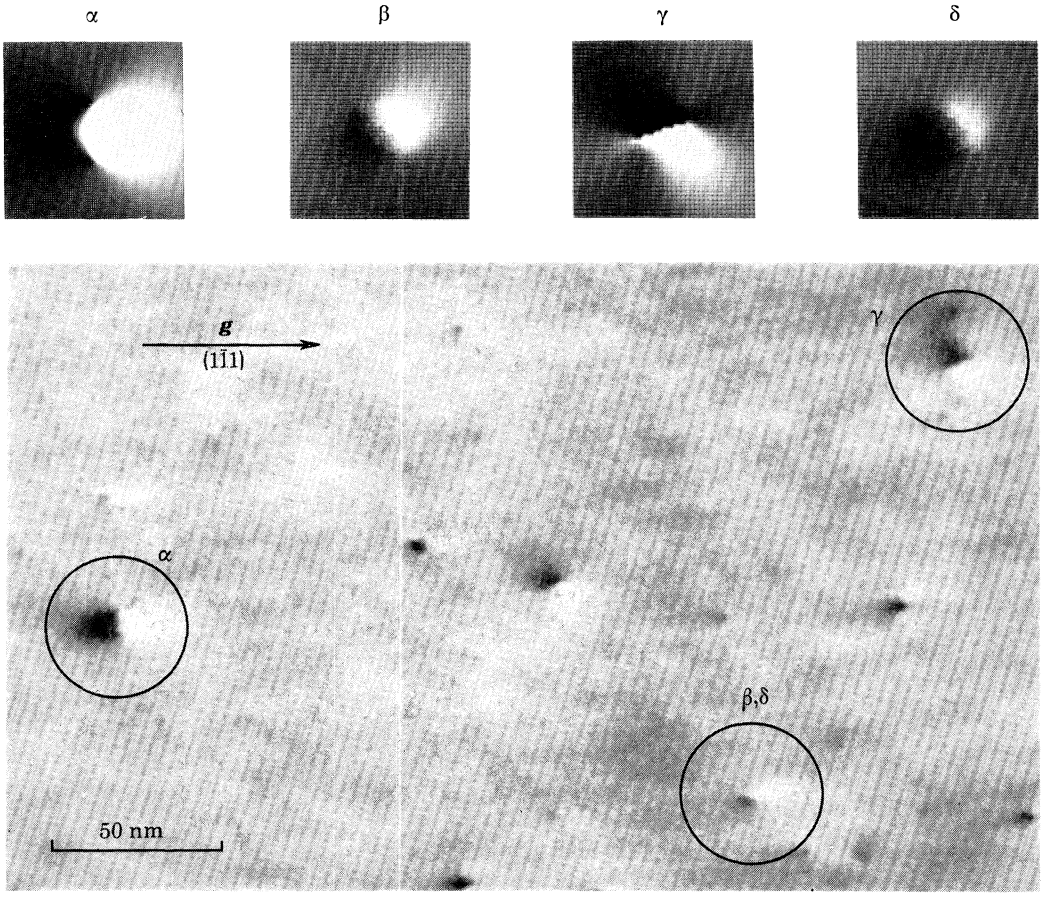

FIGURE 2. For description see opposite.

(*Facing p.* 526)

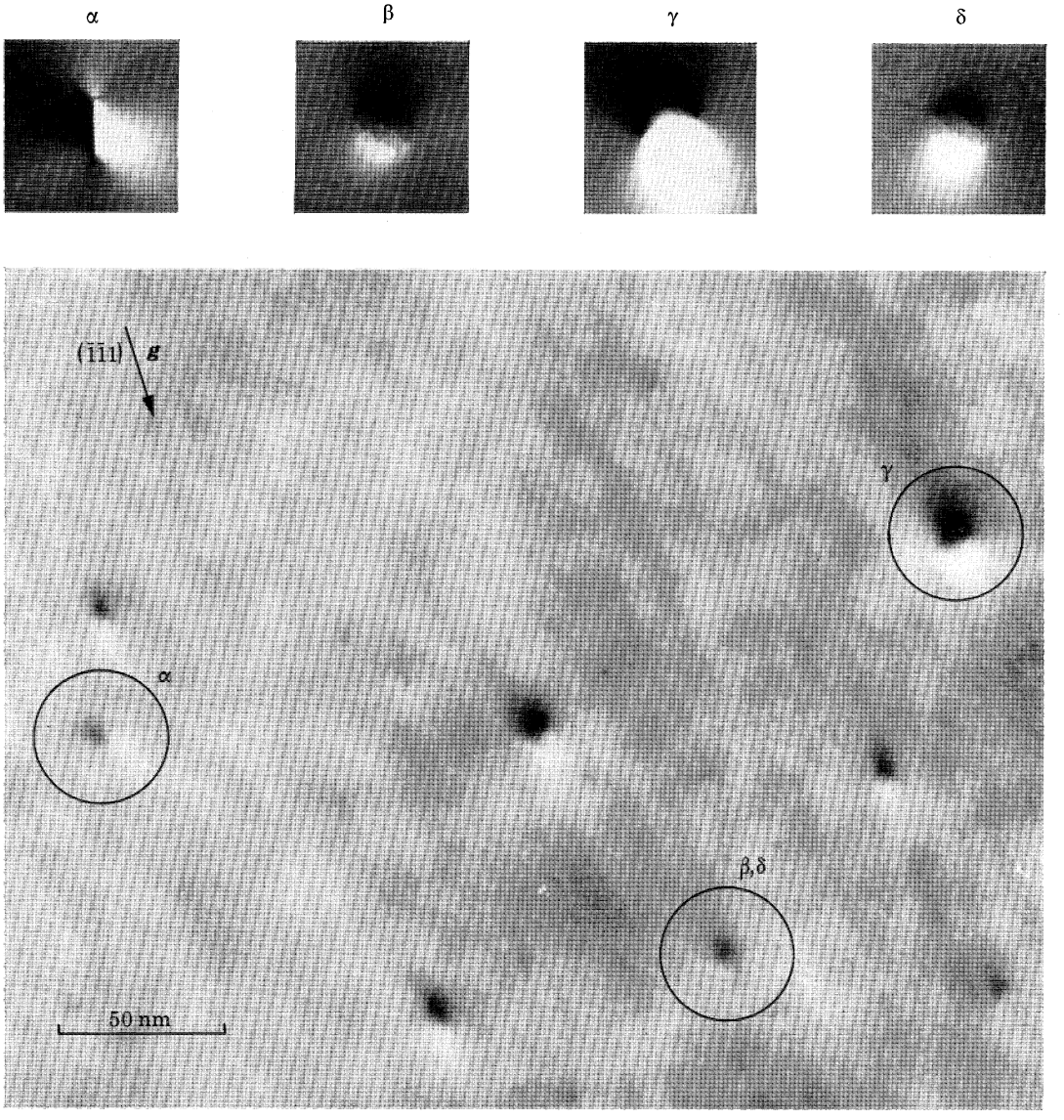

FIGURE 3. Frank loops, $\boldsymbol{g} = (\bar{1}\bar{1}1)$, Experimental image: $\boldsymbol{z} = [011]$, $\boldsymbol{N} \approx [023]$. Computed images: $\boldsymbol{z} = \boldsymbol{N} = [011]$, $t = 2\xi_g$, $(t-d) = \frac{1}{8}\xi_g$; edge length of computed images = 8.1 nm. Dark field.

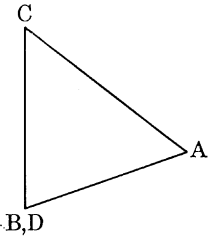

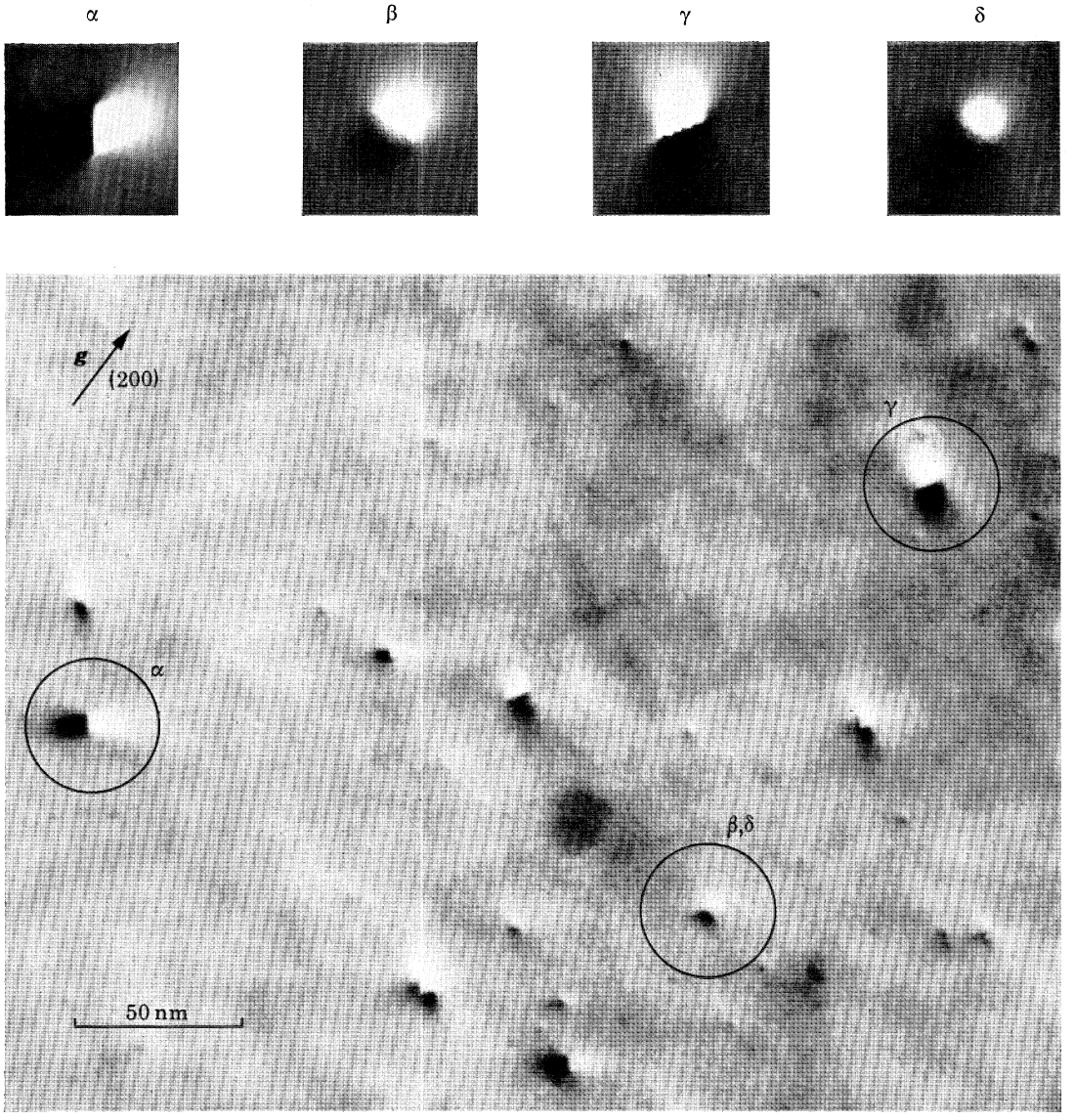

FIGURE 4. Frank loops, $\boldsymbol{g} = (200)$. Experimental image: $\boldsymbol{z} = [011]$, $\boldsymbol{N} \approx [023]$. Computed images: $\boldsymbol{z} = \boldsymbol{N} = [011]$, $t = 2\xi_g$, $(t-d) = \frac{1}{8}\xi_g$; edge length of computed images = 9.4. Dark field.

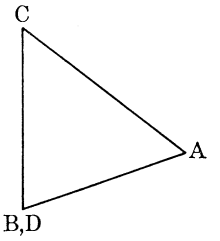

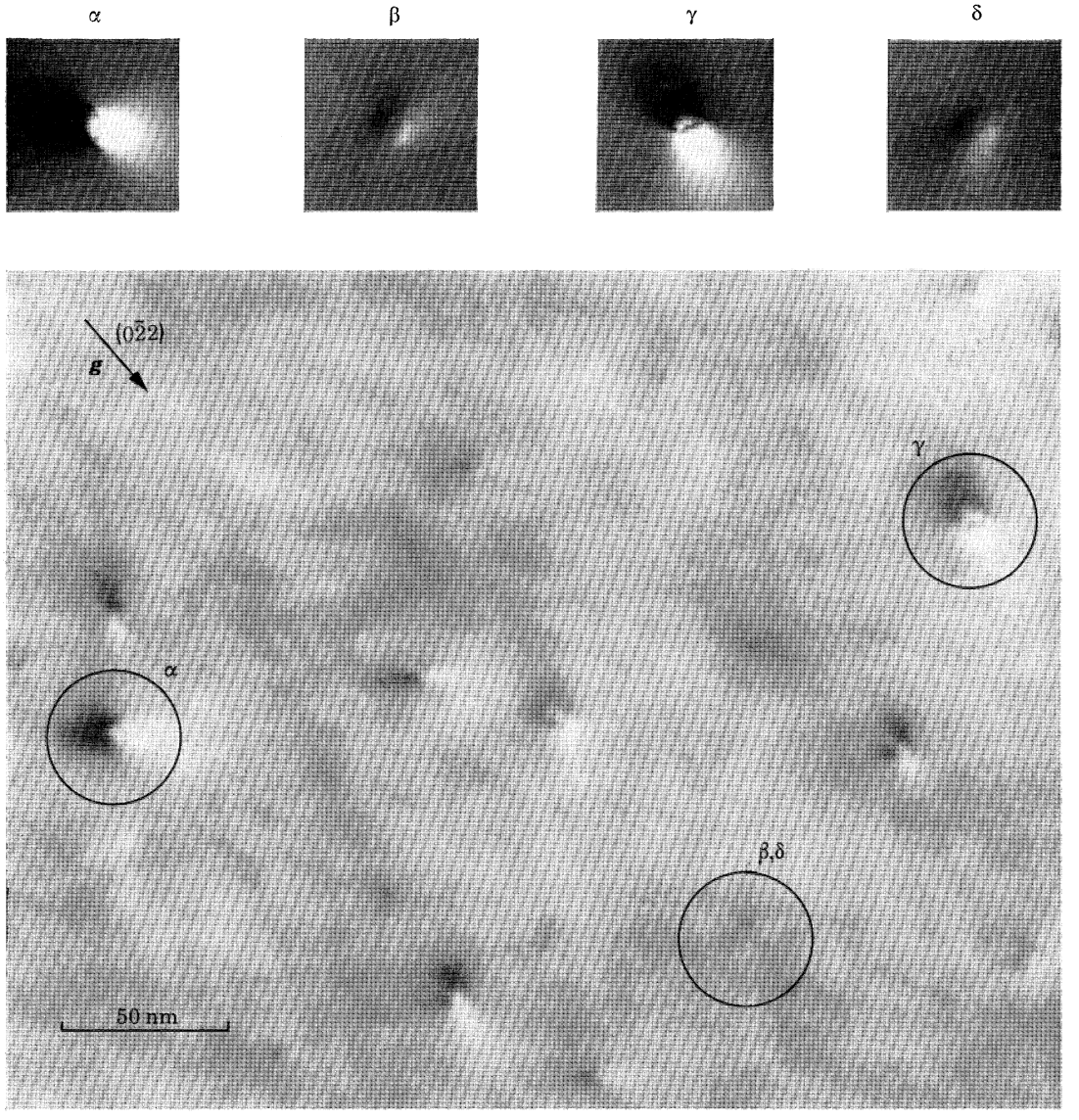

FIGURE 5. For description see opposite.

3. Experimental details

Prethinned single crystal specimens of 99.999 % pure copper and of a Cu 10 at. % Al alloy with a foil normal close to a ⟨023⟩ direction were irradiated at room temperature in a heavy-ion accelerator by 30 keV Cu^+ ions to a dose of 2×10^{11} ion cm^{-2}. Immediately after irradiation the specimens were examined in a JEM 100B electron microscope operating at 100 kV equipped with a goniometer stage. Micrographs were obtained under strong two-beam diffraction conditions for orientations near the ⟨011⟩, ⟨001⟩ and ⟨211⟩ poles. The operating reflexions were $\boldsymbol{g} = \{111\}$, $\{200\}$ and $\{220\}$ and the images studied were mainly dark field. The irradiated surface was always arranged to be the electron-exit surface in the microscope.

All experimental micrographs in this paper are of Cu specimens, except for those in figure 13 which are of a CuAl specimen.

4. Results

For all the computer-simulated images of Frank loops in this paper, the size parameter h (defined in I) was set equal to 1.5 nm. For the hexagonal loop model used, this corresponds to a diameter of about 3 nm. The contrast of small defect clusters depends on the distance of the centre of the defect from the nearest foil surface. If the quantity $\mathrm{d}\boldsymbol{R}/\mathrm{d}z$ is either symmetric or antisymmetric about the plane through the centre of the defect parallel to the image plane (where $\boldsymbol{R}$ is the value of the displacement field and z is the coordinate measured parallel to the z axis) then the product $\boldsymbol{g}\cdot\boldsymbol{l}$ reverses sign in a regular fashion as the depth of the defect in the foil is varied. In the antisymmetric case, with which we are largely concerned here, such reversals occur at distances of $\frac{1}{4}\xi_g$, $\frac{3}{4}\xi_g$ and $(\frac{1}{4}+\frac{1}{2}\mathrm{m})\,\xi_g$ from the nearby foil surfaces, where m is an integer and ξ_g is the extinction length of the operating reflexion. These distances mark the boundaries of layers of alternating signs of $\boldsymbol{g}\cdot\boldsymbol{l}$ which are labelled L1, L2, L3, ... counting away from the nearer foil surface (Ruhle 1969). (In experimental images, due to the relaxation of the strain field at the foil surfaces, the L1–L2 boundary lies at a depth of about $0.3\xi_g$). In all the computer-simulated images of this paper except those of figures 9, 10 and 11 where the variation of contrast with defect depth is studied, the centre of the defect was in the middle of the layer L1, in this case a distance of $\frac{1}{8}\xi_g$ from the electron-exit surface. The simulated images of stacking-fault tetrahedra (§ 4 *b*) were computed for a size parameter h of 2 nm, and the value of h for the non-edge loops in molybdenum (§ 4 *c*) was 2.5 nm. Thus the approximate diameter of the loops considered in molybdenum was 5 nm. The thickness of the foil is denoted by the symbol t and the depth of the

---

Description of plate 4

Figure 5. Frank loops, $\boldsymbol{g} = (0\bar{2}2)$. Experimental image: $z = [011]$, $\boldsymbol{N} \approx [023]$, Computed images: $z = \boldsymbol{N} = [011]$, $t = 2\xi_g$, $(t-d) = \frac{1}{8}\xi_g$; edge length of computed images = 14 nm. Dark field.

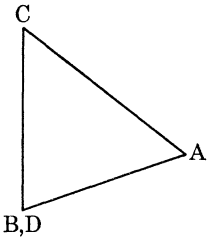

centre of the defect below the electron entry surface is denoted by d (both quantities are measured in the $-z$ direction). The quantity $(t-d)$ thus represents the height of the defect centre above the electron exit surface.

(*a*) *Images of Frank loops*

(i) *The effect of varying the operating reflexion* $\boldsymbol{g}$

(*A*) *The* $\langle 011 \rangle$ *orientation.* Figures 2–5 show dark-field micrographs of the same area of an irradiated copper foil under strong-beam conditions in four different Bragg reflexions in a dark extinction contour of a foil about $4\xi_g$ thick. In each case the z-axis is close to the direction [011] and the operating reflexions are $\boldsymbol{g} = (1\bar{1}1)$, $(\bar{1}\bar{1}1)$, (200) and $(0\bar{2}2)$ respectively. With the experimental micrograph in each case are shown computer-simulated images from approximately 3 nm diameter vacancy-type Frank loops lying on each of the four {111} planes. These planes are described by Thompson's (1953) notation on which the planes $(\bar{1}1\bar{1})$, $(1\bar{1}\bar{1})$, $(\bar{1}\bar{1}1)$ and (111) are labelled α, β, γ and δ respectively. The crystallographic orientation is indicated by the projection of the reference Thompson tetrahedron shown below the descriptions. In this orientation the line BD ([011]) is end-on with B above D. Concentrating on a particular defect (e.g. that marked γ on the experimental micrographs) good agreement with the computed images marked γ is observed for each of the reflexions. There can therefore be little doubt that this particular defect is a Frank loop lying on the (edge-on) γ plane. Similarly, it is possible to identify Frank loops on the other edge-on {111} plane, namely α. The loops are marked α on the micrographs. In each of the reflexions studied, the computed images indicated that the contrast from Frank loops on the two inclined {111} planes are very similar to each other and that therefore it would not be easy to distinguish between them. However, such images (e.g. those marked β, δ on the micrographs) are easily distinguishable from the images of edge-on loops.

TABLE 1. $|\boldsymbol{g}\cdot\boldsymbol{b}|$ VALUES, $\boldsymbol{z} = \langle 011 \rangle$

loop plane	$\boldsymbol{b}$ \ $\boldsymbol{g}\rightarrow$	$\pm(1\bar{1}1)$	$\pm(\bar{1}\bar{1}1)$	$\pm(200)$	$\pm(0\bar{2}2)$	$\pm(\bar{4}2\bar{2})$
α	$\frac{1}{3}a\langle\bar{1}1\bar{1}\rangle$	1	$\frac{1}{3}$	$\frac{2}{3}$	$\frac{4}{3}$	$\frac{8}{3}$
β	$\frac{1}{3}a\langle 1\bar{1}\bar{1}\rangle$	$\frac{1}{3}$	$\frac{1}{3}$	$\frac{2}{3}$	0	$\frac{4}{3}$
γ	$\frac{1}{3}a\langle\bar{1}\bar{1}1\rangle$	$\frac{1}{3}$	1	$\frac{2}{3}$	$\frac{4}{3}$	0
δ	$\frac{1}{3}a\langle 111\rangle$	$\frac{1}{3}$	$\frac{1}{3}$	$\frac{2}{3}$	0	$\frac{4}{3}$

Stereomicroscopy has indicated that the vast majority of defects formed by irradiation under the conditions described in § 3 lie in the layer L1 (Wilson 1969, 1971; Stathopoulos 1977). Therefore from the sign of the product $\boldsymbol{g}\cdot\boldsymbol{l}$ it was established that the defects were of vacancy type. In the case of the edge-on loops, the nature of the interface regions between the black and white lobes are in good agreement with Katerbau's (1976) predictions. For example, table 1 shows that the edge-on loops α and γ in figure 5 have a $|\boldsymbol{g}\cdot\boldsymbol{b}|$ value of $\frac{4}{3}$ (where $\boldsymbol{b}$ is the Burgers vector), and the inner structure, where there appears to be a white ring in the black lobe and a black ring in the white lobe, is clearly visible on both the experimental and computed micrographs. This feature was first noted by Eyre (1972). All other edge-on loops (in figures 2–4) are imaged under $|\boldsymbol{g}\cdot\boldsymbol{b}| \leqslant 1$ conditions and this complex interface structure is not present. However, as Katerbau predicts there are still noticeable differences in the shapes of the interface structure depending on the value of $|\boldsymbol{g}\cdot\boldsymbol{b}|$. The images for which $|\boldsymbol{g}\cdot\boldsymbol{b}| = 1$ show a curved line of no contrast, whereas on those for which $|\boldsymbol{g}\cdot\boldsymbol{b}| = \frac{1}{3}$ and $\frac{2}{3}$ this line is straight and sharp.

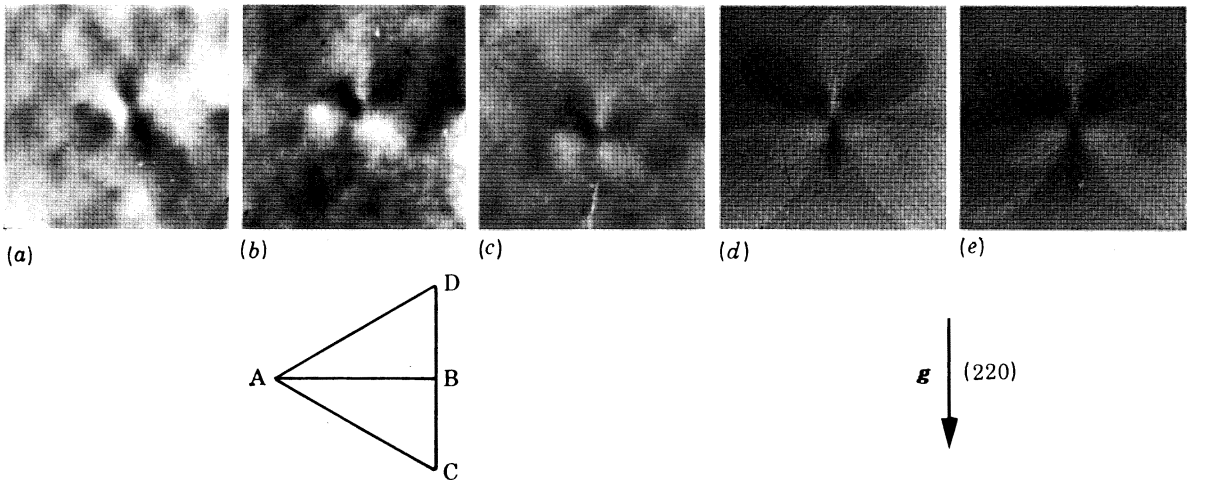

FIGURE 6. Frank loops, butterfly images. Experimental images: (*a*) Dark field $\boldsymbol{g} = (\bar{2}\bar{2}0)$, (*b*) dark field $\boldsymbol{g} = (220)$, (*c*) bright field $\boldsymbol{g} = (\bar{2}\bar{2}0)$. Loop plane α. $\boldsymbol{z} = [\bar{1}12]$, $\boldsymbol{N} \approx [023]$. Computed images: $\boldsymbol{z} = [\bar{1}12]$, $t = 4\xi_g$, $(t-d) = \frac{1}{8}\xi_g$, $\boldsymbol{g} = (220)$, $\boldsymbol{b} = \frac{1}{3}a[\bar{1}1\bar{1}]$, $\boldsymbol{g}\cdot\boldsymbol{b} = 0$; (*d*) $\boldsymbol{N} = [\bar{1}12]$, (*e*) $\boldsymbol{N} = [023]$. Edge length of experimental images = 50 nm; edge length of computed images = 14 nm.

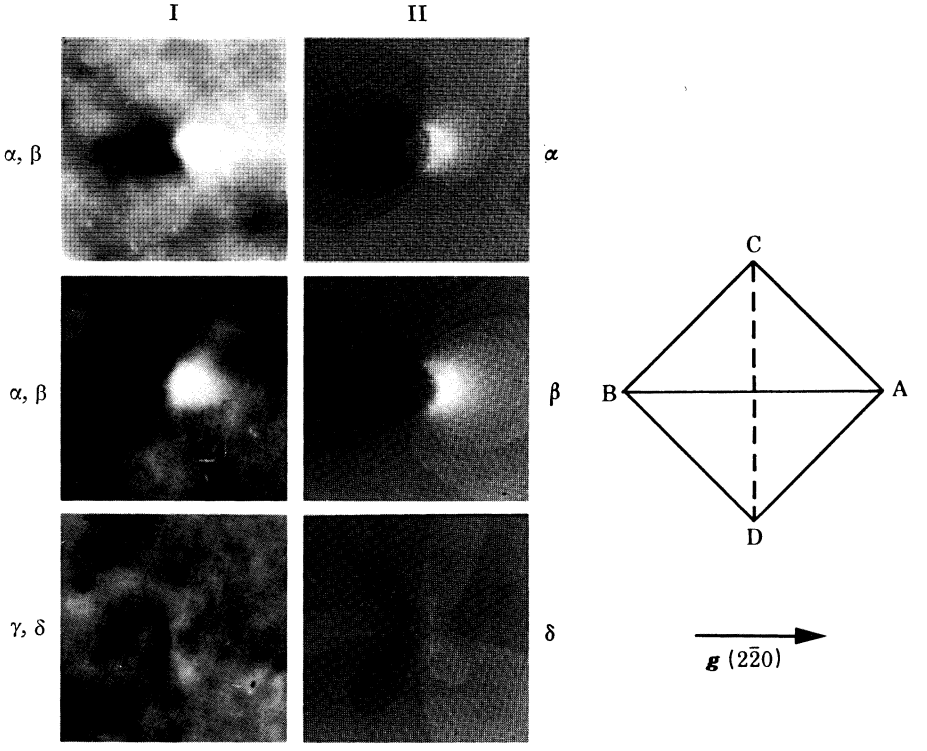

FIGURE 8. Frank loops, images at [001] orientation, $\boldsymbol{g} = (2\bar{2}0)$. Column I: Experimental images: $\boldsymbol{z} = [001]$, $\boldsymbol{N} \approx [023]$. Column II: Computed images: $\boldsymbol{z} = [001]$, $\boldsymbol{N} = [023]$, $t = 4\xi_g$, $(t-d) = \frac{1}{8}\xi_g$. Edge length of experimental images = 50 nm; edge length of computed images = 14 nm. Dark field.

(*Facing p.* 528

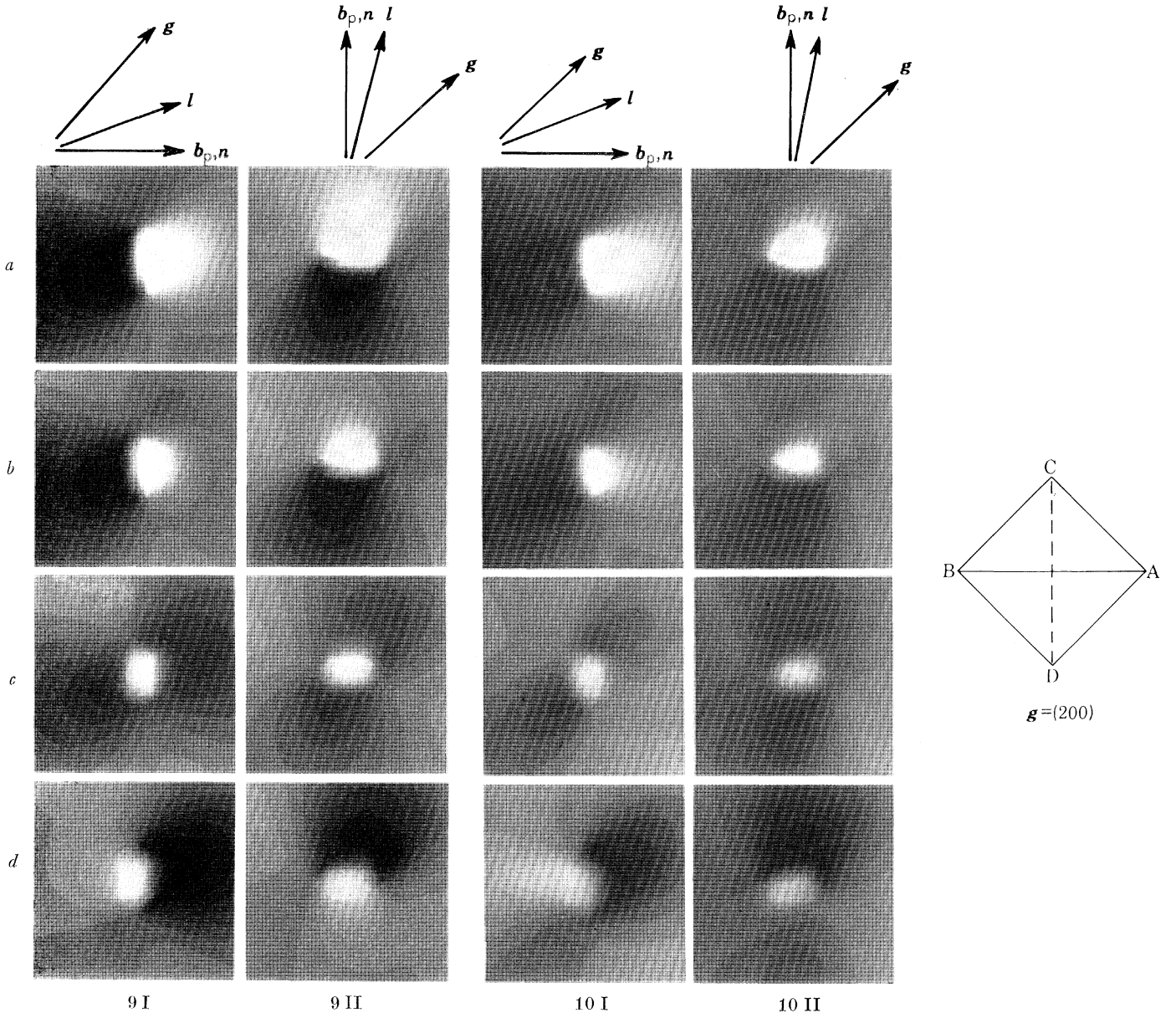

FIGURE 9. Frank loops, dependence of contrast on depth, $\boldsymbol{g} = (200)$. Computed images: $\boldsymbol{z} = \boldsymbol{N} = [001]$, $t = 4\xi_g$; (*a*) $(t-d) = \frac{1}{8}\xi_g$; (*b*) $(t-d) = \frac{3}{16}\xi_g$; (*c*) $(t-d) = \frac{1}{4}\xi_g$; (*d*) $(t-d) = \frac{5}{16}\xi_g$. Column I: loop plane α; column II: loop plane δ. Edge length of images = 8.2 nm. Dark field.

FIGURE 10. Frank loops, dependence of contrast on depth. $\boldsymbol{N} = [023]$. All other parameters same as for figure 9.

DESCRIPTION OF PLATE 7

FIGURE 11. Frank loops, measurement of loop size, $\boldsymbol{g} = (1\bar{1}1)$. Column I: experimental images (θ = foil tilt): (*a*) $\theta = 0°$, $(t-d) = 4.45 \pm 0.45$ nm, (*b*) $\theta = 10°$, $(t-d) = 4.51 \pm 0.45$ nm. (*c*) $\theta = 20°$, $(t-d) = 4.74 \pm 0.45$ nm, (*d*) $\theta = 44°$, $(t-d) = 6.17 \pm 0.62$ nm, (*e*) $\theta = 53°$, $(t-d) = 7.40 \pm 0.74$ nm. Computed images: $\boldsymbol{z} = \boldsymbol{N} = [011]$, (*a*) $(t-d) = 3.8$ nm, (*b*) $(t-d) = 4.6$ nm, (*c*) $(t-d) = 4.8$ nm, (*d*) $(t-d) = 6.1$ nm, (*e*) $(t-d) = 6.8$ nm. Column II: $t = 2\xi_g$, column III: $t = 2.5\xi_g$. Edge length of experimental images = 64 nm, edge length of simulated images = 8.2 nm. Dark field.

FIGURE 12. Frank loops, dependence of contrast on deviation parameter. Computed images; $\boldsymbol{z} = \boldsymbol{N} = [011]$, $\boldsymbol{g} = (200)$, $t = 4\xi_g$, $(t-d) = \frac{1}{8}\xi_g$. Columns I and III: bright-field. Columns II and IV: dark field. Columns I and II: loop plane α (edge-on loop). Columns III and IV: loop plane δ (inclined loop). Row (*a*) $w = 0$; (*b*) $w = 0.2$; (*c*) $w = 0.4$; (*d*) $w = 0.6$; (*e*) $w = 0.8$; (*f*) $w = 1.0$. Edge length of images = 9.5 nm.

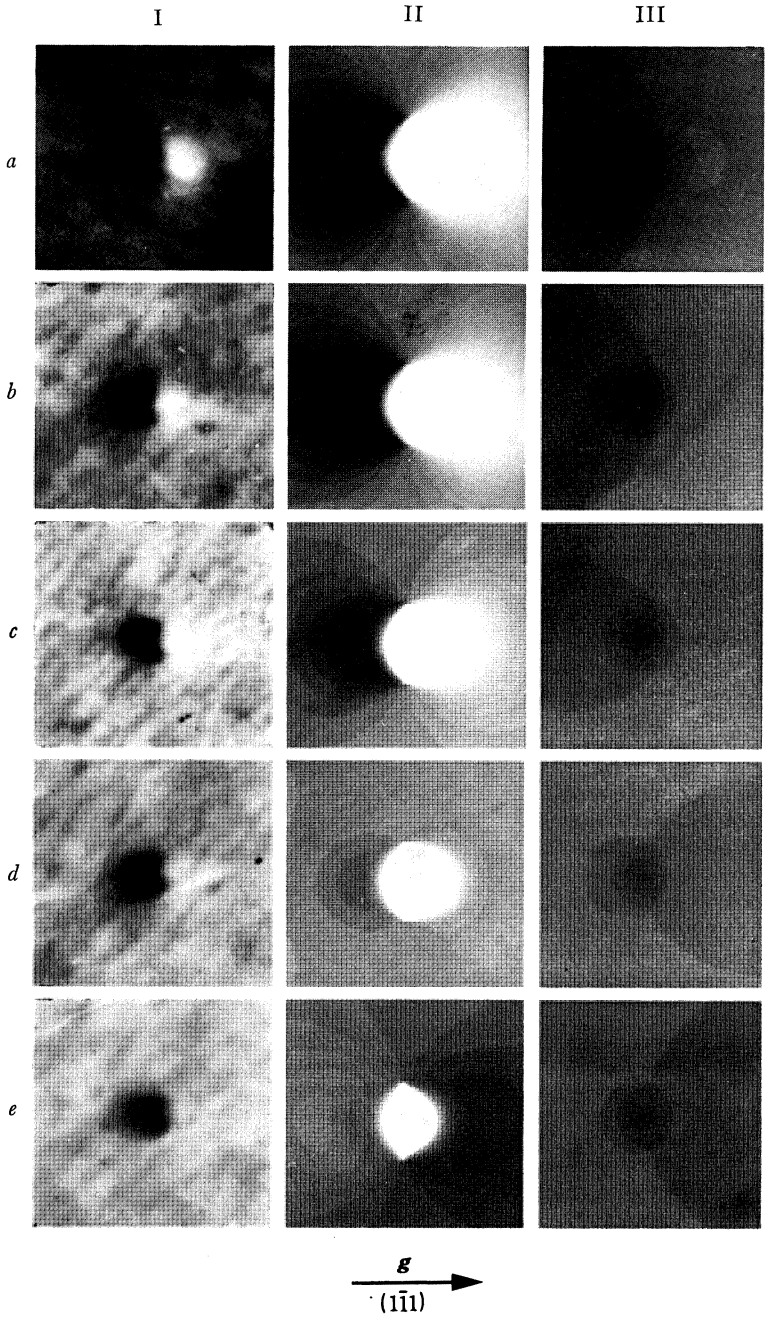

FIGURE 11. For description see opposite.

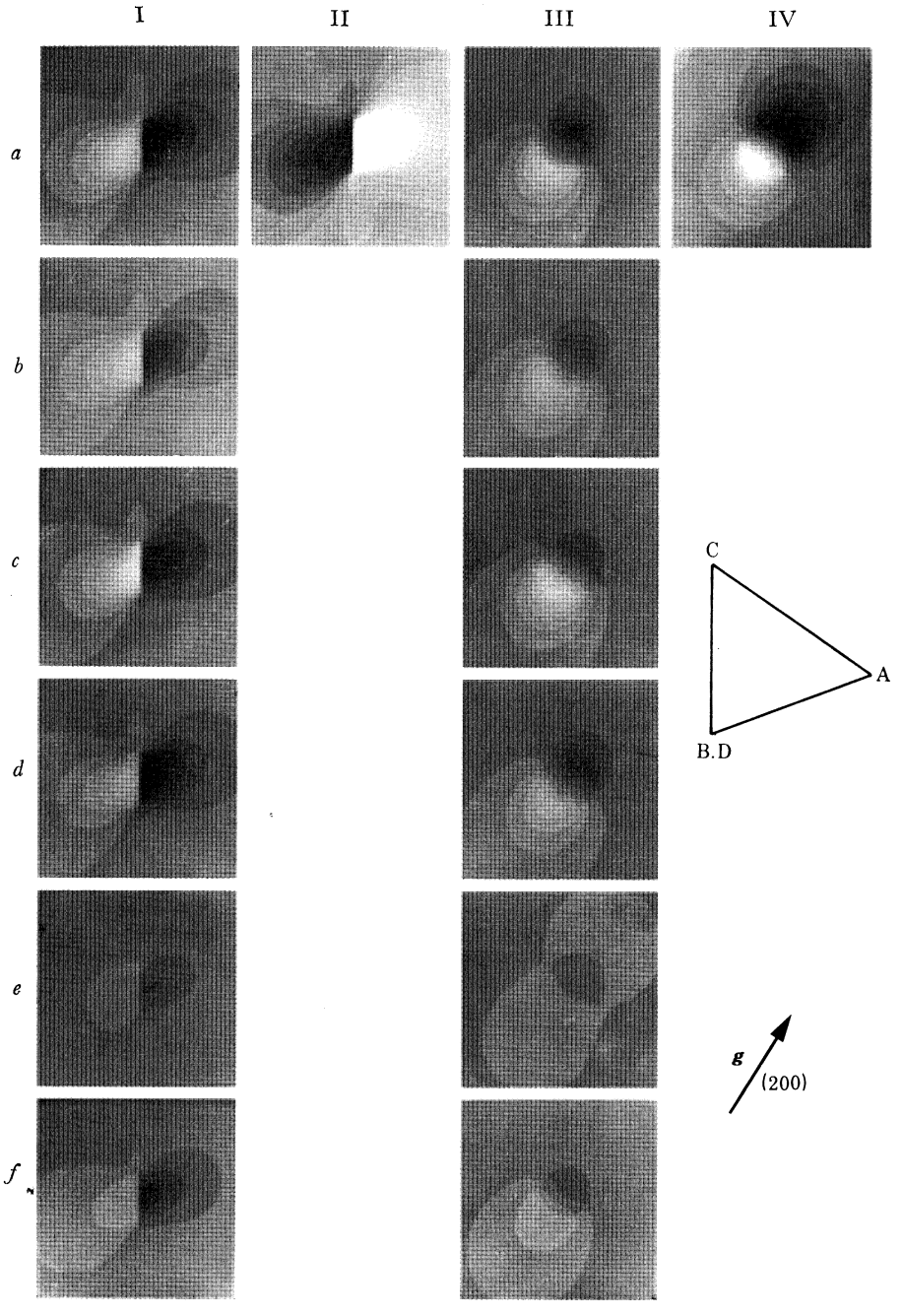

FIGURE 12. For description see opposite.

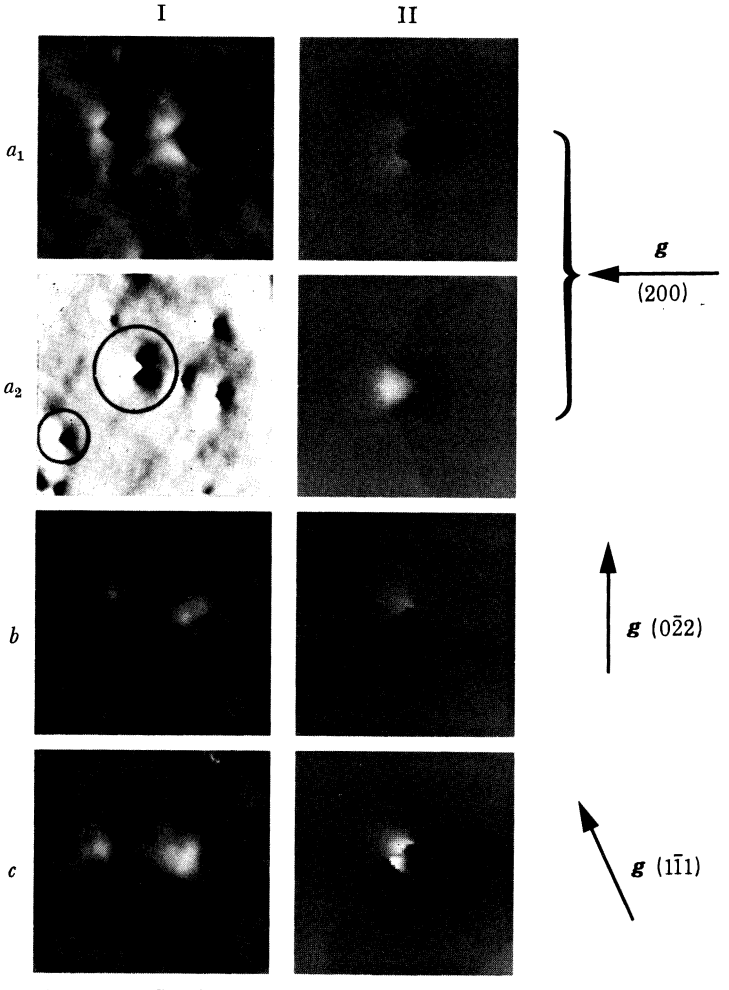

FIGURE 13. Stacking-fault tetrahedra, $\boldsymbol{z} = [011]$. (a_1) Orientation 1, $\boldsymbol{g} = (200)$; (a_2) orientation 2, $\boldsymbol{g} = (200)$; (b) orientation 1, $\boldsymbol{g} = (0\bar{2}2)$; ($c$) orientation 1, $\boldsymbol{g} = (1\bar{1}1)$. Column I : Experimental images: $\boldsymbol{N} \approx [023]$. Column II: Computed images: $\boldsymbol{N} = [023]$, $t = 4\xi_g$, $(t-d) = \frac{1}{8}\xi_g$. Edge length of experimental images = 114 nm, edge length of computed images = 14 nm. Dark field.

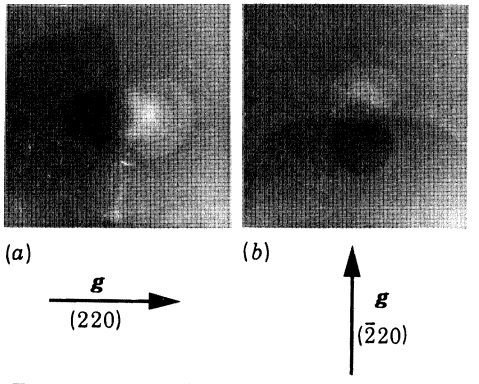

FIGURE 14. Stacking-fault tetrahedron $\boldsymbol{z} = [001]$. Orientation 2. Computed images: $\boldsymbol{N} = [023]$, $t = 4\xi_g$, $(t-d) = \frac{1}{8}\xi_g$. (a) $\boldsymbol{g} = (220)$, (b) $\boldsymbol{g} = (2\bar{2}0)$. Edge length of images = 14 nm. Dark field.

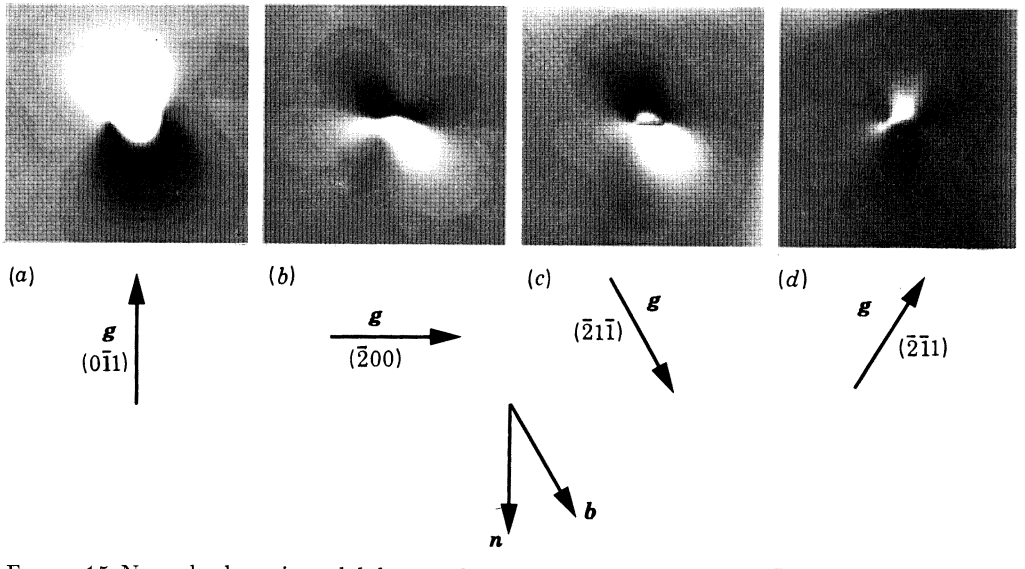

FIGURE 15. Non-edge loops in molybdenum. Computed images: $\boldsymbol{b} = (a/2)\,[\bar{1}1\bar{1}]$, $\boldsymbol{n} = [01\bar{1}]$, $t = 2\xi_g$, $(t-d) = \frac{1}{8}\xi_g$. (a) $\boldsymbol{z} = \boldsymbol{N} = [\bar{1}55]$, $\boldsymbol{g} = (0\bar{1}1)$; ($b$) $\boldsymbol{z} = \boldsymbol{N} = [023]$, $\boldsymbol{g} = (\bar{2}00)$; ($c$) $\boldsymbol{z} = \boldsymbol{N} = [\bar{1}35]$, $\boldsymbol{g} = (\bar{2}1\bar{1})$; ($d$) $\boldsymbol{z} = \boldsymbol{N} = [\bar{1}53]$, $\boldsymbol{g} = (\bar{2}\bar{1}1)$. Edge length of images: (a) 20.8 nm; (b) 29.5 nm; (c), (d) 36.8 nm. Dark field.

(*B*) '*Butterfly*' *images.* When a Frank loop in an edge-on orientation is imaged under conditions for which $|\boldsymbol{g}\cdot\boldsymbol{b}| = 0$, the type of contrast figure known as a 'butterfly' image results. This is an image consisting of six alternate black and white lobes about the centre of the contrast figure. The general conditions for the formation of such an image are given in the appendix.

At the $[\bar{1}12]$ orientation, $|\boldsymbol{g}.\boldsymbol{b}| = 0$ for a Frank loop with $\boldsymbol{b} = \frac{1}{3}a[\bar{1}1\bar{1}]$ observed in $\boldsymbol{g} = (220)$. A bright-field and two dark-field butterfly images are shown in figure 6. It can be seen that the corresponding bright- and dark-field images are complementary, in agreement with the usual rule for defects near the electron exit surface of the foil. The extra complication in this image is the fact that the foil normal $\boldsymbol{N} = [023]$ is inclined by an angle of about 25° to $\boldsymbol{z}$. If $\boldsymbol{N}$ had been parallel to $\boldsymbol{z}$ the dark-field (220) image would be similar to the simulated image on the left, i.e. it would be symmetric about a line parallel to $\boldsymbol{g}$ through the centre of the image. In fact none of the experimental images show this symmetry. The right hand computed image (for which $\boldsymbol{N} = [023]$), shows that the breaking of this symmetry is at least partly due to the tilt of the foil surfaces.

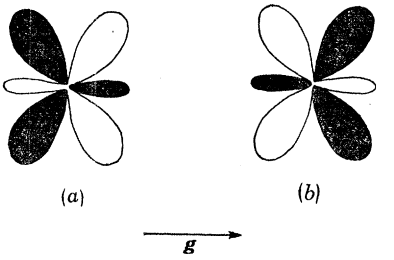

FIGURE 7. Butterfly images of edge-on Frank loop. ($|\boldsymbol{g}\cdot\boldsymbol{b}| = 0$). (*a*) Vacancy loop, (*b*) interstitial loop.

It has been found that the character (i.e. whether vacancy-type or interstitial-type) of loops giving rise to butterfly images can be determined in a manner similar to that for non-zero $|\boldsymbol{g}\cdot\boldsymbol{b}|$ images, i.e. by observing the positions of the black and white lobes of the contrast figure relative to the direction of the $\boldsymbol{g}$ vector for a loop of known depth in the foil. The difference is that in this case there are six alternate black and white lobes. Figure 7 illustrates schematically dark-field images expected from an edge-on Frank loop whose distance from the nearest foil surface places it in the layer L1. If the $\boldsymbol{l}$-vector is defined as the line joining the weighted centre of the black regions to that of the white regions then the character of the loop may be determined from the rule given by Ruhle (1969). This states that for loops in odd numbered layers (i.e. L1, L3, ..., etc.) if $\boldsymbol{g}\cdot\boldsymbol{l} > 0$ the loop is of vacancy type and if $\boldsymbol{g}\cdot\boldsymbol{l} < 0$ it is of interstitial type. From figure 7 it may be seen that the weighted centre of the black lobes lies in the small white lobe and vice versa and that $\boldsymbol{l}$ is either parallel to or antiparallel to $\boldsymbol{g}$. If a vector $\boldsymbol{l}'$ is defined as that joining the centre of the small black lobe to that of the small white one, then this vector is antiparallel to $\boldsymbol{l}$. This is explained by the following argument: the intensities in the small lobes are determined by the component of the displacement field in the direction of $\boldsymbol{g}$ near the plane of the loop (in this case also parallel to $\boldsymbol{g}$). The expressions for the displacement field given in the appendix show that this component is directed away from the loop for vacancy loops and towards it for interstitial loops. The opposite is true for the parts of the displacement field contributing to the larger lobes.

(*C*) *The* ⟨001⟩ *orientation.* When viewed at the ⟨001⟩ orientation, all Frank loops are equally inclined. Table 2 shows that when a {220} operating reflexion is used, loops on two of the {111}

planes are imaged with $|\boldsymbol{g}\cdot\boldsymbol{b}| = 0$ and two with $|\boldsymbol{g}\cdot\boldsymbol{b}| = \frac{4}{3}$. Figure 8 illustrates Frank loops in a foil with $\boldsymbol{N} = [023]$ viewed at the [001] orientation in the $(2\bar{2}0)$ reflexion. Computed images of loops lying on the Thompson planes α, β and δ are shown. The image of the loop on the γ plane is expected to be similar to that of the loop on the δ plane except for a reflexion about a line parallel to the $\boldsymbol{g}$ vector through the centre of the contrast figure. This does not obtain exactly because the foil normal is inclined to $\boldsymbol{z}$ by about 34°. This is also the reason for the images α, β being not quite symmetric about a line parallel to the $\boldsymbol{g}$-vector through their centres. What is quite clear, however, is the fact that under such conditions loops on two of the {111} planes show up with strong black–white contrast while loops on the other two {111} planes are visible only faintly, giving rise to what might be described as distorted butterfly images. Viewing the same loops in the orthogonal (220) reflexion causes this pattern to reverse, i.e. the loops which showed up weakly in the $(2\bar{2}0)$ reflexion now exhibit strong black–white contrast and vice versa. This result is useful as a method of distinguishing black–white images of Frank loops and stacking-fault tetrahedra at this orientation (see § 4*b* (ii)). Another feature of the images marked α, β in figure 8 is the complicated structure of the black–white interface, showing features not unlike those in figure 5. We see therefore that the rule that such a complex structure is expected for $|\boldsymbol{g}\cdot\boldsymbol{b}| > 1$ seems to be true even for inclined loops.

TABLE 2. $|\boldsymbol{g}\cdot\boldsymbol{b}|$ VALUES, $\boldsymbol{z} = \langle 001\rangle$

loop plane	$\boldsymbol{b}$ \ $\boldsymbol{g}\rightarrow$	± (200)	± (020)	± $(2\bar{2}0)$
α	$\frac{1}{3}a\langle\bar{1}1\bar{1}\rangle$	$\frac{2}{3}$	$\frac{2}{3}$	$\frac{4}{3}$
β	$\frac{1}{3}a\langle 1\bar{1}\bar{1}\rangle$	$\frac{2}{3}$	$\frac{2}{3}$	$\frac{4}{3}$
γ	$\frac{1}{3}a\langle\bar{1}\bar{1}1\rangle$	$\frac{2}{3}$	$\frac{2}{3}$	0
δ	$\frac{1}{3}a\langle 111\rangle$	$\frac{2}{3}$	$\frac{2}{3}$	0

(ii) *Depth dependence of images*

Even in ion-irradiated foils the small loops do not always lie in the layer L1 and a substantial number may lie in the region of the boundary between the layers L1 and L2. In experiments involving counting the number of loops in a certain area of a micrograph therefore, it is important to understand the image contrast of loops in the L1–L2 interface region and of those just within the layer L2. Figure 9 indicates the contrast expected from a foil in a [001] orientation with $\boldsymbol{N}$ parallel to $\boldsymbol{z}$, and a (200) operating reflexion. Relaxation of the strain fields due to the nearby foil surface is not taken into account and the L1–L2 boundary occurs at a depth of $\frac{1}{4}\xi_{\boldsymbol{g}}$ (in this case about 7 nm) from the foil surface. A gradual decrease in the size of the contrast figure as the L1–L2 boundary is approached is seen, as well as the reversal of the sign of $\boldsymbol{g}\cdot\boldsymbol{l}$ in L2. It had been believed for some time (see, for example, Ruhle 1969) that loops in the L1–L2 boundary give rise to black-dot images. This is not observed in these simulated images. On the contrary, in this case the complicated black–white–black image also obtained by Katerbau (1976) is seen. Even in the case of the edge-on loop (for computations performed for the [011] orientation) a residual black–white contrast is obtained.

In figure 10, a similar series of computed images is shown, the only difference being that the calculations were done for a [023] foil normal. The distance traversed in the foil by the electron beam was the same as for the case of figure 8. (This means, of course, that the thickness of the foil measured in the direction normal to its surface is less than in the former case.) The angle

between $\boldsymbol{N}$ and $\boldsymbol{z}$ in this case is also about 34°, and the importance of taking this into account may be judged by comparing the two figures. It is clear that the directions of the $\boldsymbol{l}$- vectors can differ by large angles.

(iii) *Loop size*

It is often required to determine the diameter of a small dislocation loop from its electron microscope images. Columns II and III of figure 11 illustrate computed images of a small edge-on Frank loop at different depths in foils of thickness 2 and 2.5 ξ_g respectively. In each case the distance of the loop centre from the electron-exit surface of the foil lies in the range from the middle of the layer L1 to the L1–L2 boundary. In the case of column II, although the size of the contrast figure decreases as the loop centre approaches the L1–L2 boundary, the width of the black–white interface region is constant. Measurement shows that this width is equal to the projected diameter of the loop. At the L1–L2 boundary the black lobe of the contrast figure has almost disappeared and the image appears in the form of a white spot (i.e. figure 11, II (*d*)).

Corresponding images in column III show much lower contrast, as would be expected, since the background (i.e. perfect crystal) intensity is at a maximum in the dark-field image for such a thickness. The $\boldsymbol{l}$-vector is in the same direction as in column II but as the L1–L2 boundary is approached, the image tends to a black spot. In this case too, however, if the image width is measured in the same sense as before, it is effectively constant and equal to the projected diameter of the loop.

These results imply that in the case of edge-on Frank loops their projected diameters may be measured directly on micrographs without detailed knowledge of their depths in the foil, provided thay are in the layer L1 or near the L1–L2 boundary. Regarding the difference in columns II and III of the contrast near the L1–L2 boundary, Katerbau (1976) has shown that for such depths of the defect, the contrast is determined mainly by the 'void term' in his expressions which indicate that as the foil thickness is increased the sign of this term oscillates with a period of about an extinction length, thus providing the explanation.

Column I shows experimental images of a defect whose effective depth in the foil (measured in the direction of the electron beam) is varied by tilting the foil about $\boldsymbol{g}$ (and in this case also about $\boldsymbol{b}$). The tilt also increases the effective thickness of the foil so that although the upper images in this column may correspond closely to the upper ones of column II, the lower images would correspond to the lower ones of column III. This appears to be the case, as the upper images show strong black–white contrast while the lower ones tend to a black dot.

(iv) *Dependence on deviation parameter*

The difficulty in setting up exact strong-beam conditions in electron microscope experiments makes it important to know the precise variation of the image contrast of a small centre of strain with the deviation parameter w ($= s\xi_g$, where s is the excitation error of the operating reflexion). Figure 12 illustrates this variation in the bright-field images for an edge-on Frank loop and for an inclined Frank loop in a foil of thickness $4\xi_g$, at an $\langle 011 \rangle$ orientation under symmetric Laue conditions. Also shown are the dark-field images for $w = 0$. The first point to notice is that the dark-field images show higher contrast for this particular thickness. This can be understood by the following argument: let the background (perfect crystal) intensities in bright- and dark-field be I_0^b and I_1^b respectively and let the change in intensity caused by the presence of the defect be ΔI. If ΔI is roughly the same in both bright- and dark-field then the contrast in each of these

modes is given by $\Delta I/I_0^b$ and $\Delta I/I_1^b$ respectively. But for $t = n\xi_g$ (t is the foil thickness in the direction of the electron beam and n is an integer), $I_1^b < I_0^b$. Therefore for such thickness there is more contrast in the dark-field image than in the bright-field image. The situation is reversed for $t = (n+\frac{1}{2})\,\xi_g$. In fact it is found that contrast is highest in the dark extinction contours in both the bright-field and the dark-field images making these the most convenient regions from which to study the contrast of small centres of strain.

Regarding the contrast variation with w on the bright-field images, it is found that as w is increased from zero the contrast initially decreases to reach a minimum near $w = 0.2$, then rises to a maximum around $w = 0.4$–0.6, decreases to a minimum near 0.8 and then rises again slightly near $w = 1.0$. Comparison with the bright-field rocking curve for a perfect crystal (Hirsch *et al.* 1965) of thickness $4\xi_g$ indicates that maxima in contrast correspond to minima in I_0^b and vice versa, thus indicating that the percentage variation of ΔI with w is much smaller that that of I_0^b. This conclusion seems to be verified by figure 12. Reducing the thickness increases the oscillation period of $I_0^b(w)$. A computer-simulation study of the contrast variation with w in a foil thickness $2\xi_g$ confirmed this prediction. All these observations may be understood by a theory based on the kinematical scattering of Bloch waves generalized to the case where $w \neq 0$ (Katerbau 1978).

(*b*) *Images of stacking-fault tetrahedra*

Resolvable electron microscope images of stacking-fault tetrahedra have been observed by Silcox & Hirsch (1959), Chik (1966), Jenkins (1974) and many others. In these cases the defect is imaged primarily by the characteristic stacking-fault contrast from the faces for which $\boldsymbol{g}\cdot\boldsymbol{R}'$ is non-zero (where $\boldsymbol{R}'$ is the fault vector) For a small tetrahedron imaged under strong-beam conditions, however, the stacking-fault contrast may not be directly visible and it is necessary to rely on the contrast from its strain field. Interpretation of such contrast has so far been hampered by a lack of a theoretical model for the strain field of the stacking-fault tetrahedron. The strain-field model described in I has therefore been used to produce computer-simulated images of tetrahedra imaged under different low-order (strong-beam) reflexions to aid in the interpretation of contrast features from small defects in a Cu^+ ion irradiated Cu–Al alloy. The low stacking-fault energy of the alloy leads us to expect that the Frank loops initially formed after vacancy collapse near the centre of a collision cascade would tend to dissociate fully to form tetrahedra by the Silcox–Hirsch (1959) mechanism.

(i) *The* $\langle 011 \rangle$ *orientation*

The geometric projection of a tetrahedron onto the image plane for this orientation is a triangle. A stacking-fault tetrahedron can exist in two possible orientations depending on the manner of dissociation of the original Frank loop, and the projections of these two orientations onto the image plane are related by a rotation of 180° about the $\boldsymbol{z}$ axis. Figure 13a_1, b and c illustrate images of a tetrahedron in one of these orientations (say, orientation 1) while figure 13a_2 shows a tetrahedron in the other orientation (orientation 2). The most striking result is that black–white contrast is observed even in the low order {111} and {200} reflexions, contrary to the result of Chik (1966). The defects are clearly identifiable by comparison with the simulated images shown. The black–grey–white contrast in the {022} reflexion is observed. The direction of the $\boldsymbol{l}$ vector, defined loosely as the line joining the weighted centres of the black and white regions, is seen to lie near that of the the corresponding $\boldsymbol{g}$ vector. The sign of $\boldsymbol{g}\cdot\boldsymbol{l}$ was found to reverse in the case of the interstitial-type tetrahedron in the same layer thus enabling the charac-

ter of a tetrahedron to be determined by essentially the same methods as for a Frank loop (if its depth in the foil is known). In fact, an interstitial tetrahedron in orientation 1 would give rise to an image similar to that of a vacancy tetrahedron in orientation 2 (figure $13a_2$) except for a rotation about $\boldsymbol{z}$ by 180° (neglecting small differences due to the fact that $\boldsymbol{N}$ may not be quite parallel to $\boldsymbol{z}$).

(ii) *The* $\langle 001 \rangle$ *orientation*

Computer-simulated images of a vacancy-type tetrahedron at this orientation observed in the orthogonal {220} reflexions are shown in figure 14. Both images show normal black–white contrast with the direction of $\boldsymbol{l}$ close to that of $\boldsymbol{g}$. This observation could form the basis of a method of distinguishing the images of Frank loops and tetrahedra at this orientation (P. B. Hirsch 1975, private communication). It was indicated in §4*a*(*i*C) that when a Frank loop at the same orientation is imaged in orthogonal {220} reflexions it shows up in strong black–white contrast in one reflexion and very weak distorted 'butterfly' contrast in the other. Thus tetrahedra and Frank loops could be easily distinguished by comparing images of the same defect in the orthogonal {220} reflexions at the $\langle 001 \rangle$ orientation.

(*c*) *Images of loops with non-edge character*

Self-ion irradiation of the b.c.c. metal molybdenum is thought to give rise initially to vacancy loops on the densely packed $\langle 110 \rangle$ planes. These faulted loops, however, have a tendency to unfault because of the high stacking-fault energy. The Burgers vector $\boldsymbol{b}$ of the loop is converted to a perfect lattice vector by one of the following reactions (Eyre & Bullough 1965):

$$\tfrac{1}{2}a\langle 110\rangle + \tfrac{1}{2}a\langle 001\rangle \rightarrow \tfrac{1}{2}a\langle 111\rangle,$$
$$\tfrac{1}{2}a\langle 110\rangle + \tfrac{1}{2}a\langle 1\bar{1}0\rangle \rightarrow a\langle 100\rangle.$$

The loops with $\boldsymbol{b} = a\langle 100\rangle$ are the subject of another paper (English *et al.* 1978). Of the loops with $\boldsymbol{b} = \frac{1}{2}a\langle 111\rangle$, the ones most likely to be observed in the electron microscope are those for which $\boldsymbol{b}$ is perpendicular to $\boldsymbol{z}$ (loops with other Burgers vectors may glide out of the foil). The theoretically expected contrast from such loops have been studied by Haussermann *et al.* (1972) using an infinitesimal loop model, by Saldin & Whelan (1975) and Saldin *et al.* (1978*a*) using the angular dislocation model, by Ohr (1973) and by Holmes *et al.* (1976) using a circular loop model. The simulated images in figure 15 are in agreement with the results of the last named of the above authors thus indicating the equivalence for such purposes of images computed from the circular loop model and from the angular dislocation model. In particular the contrast feature mentioned in §4*a*(*i*A) in the black–white interface region for $1 < |\boldsymbol{g}\cdot\boldsymbol{b}| < 2$ can be seen in figure 15*c*. As a consequence of using the infinitesimal loop model, Hausserman *et al.* (1972) concentrated on the long-range parts of the contrast figure and classified the image types as 'normal', 'weakly distorted', 'strongly distorted' and 'butterfly' images. This model is neither capable of accurately simulating the image contrast in the interface region nor is it of use for the determination of the sizes of loops. Holmes *et al.* (1976), however, concentrated on the interface structure and the $|\boldsymbol{g}\cdot\boldsymbol{b}|$ criterion. As a system of classifying the images, however, the $|\boldsymbol{g}\cdot\boldsymbol{b}|$ criterion has its drawbacks as can be seen by comparing the $|\boldsymbol{g}\cdot\boldsymbol{b}| = 1$ images (*a*) and (*b*) which are clearly of distinguishable type. The reason, of course, is that with non-edge loops, the loop normal $\boldsymbol{n}$ is just as important a parameter as the Burgers vector $\boldsymbol{b}$ in determining the form of the image.

5. Direction of the black–white streaking

The direction of the black–white streaking vector $\boldsymbol{l}$ relative to those of $\boldsymbol{g}$, $\boldsymbol{b}_{\text{proj}}$ and $\boldsymbol{n}_{\text{proj}}$ (where $\boldsymbol{b}_{\text{proj}}$ and $\boldsymbol{n}_{\text{proj}}$ are the projections of the Burgers vector $\boldsymbol{b}$ and the loop normal $\boldsymbol{n}$ on the image plane) has been the subject of discussion by a number of authors (e.g. Ruhle *et al.* 1965; Yoffe 1970, 1972; McIntyre *et al.* 1970; Eyre *et al.* 1977*b*; Ohr 1976, 1978). If α, β and γ are the angles between $\boldsymbol{g}$ and $\boldsymbol{l}$, $\boldsymbol{g}$ and $\boldsymbol{b}_{\text{proj}}$ and $\boldsymbol{g}$ and $\boldsymbol{n}_{\text{proj}}$ respectively, Ohr (1976) proposed the relation $\alpha = \frac{1}{3}(\beta+\gamma)$ for loops in isotropic media. All our computer-simulated images of dislocation loops observed under symmetric Laue conditions obeyed this rule but discrepancies were found when the foils were imaged under non-symmetric Laue conditions as described in §4*a*(ii). For edge-on loops in highly anisotropic materials, the directions of $\boldsymbol{l}$ and $\boldsymbol{b}$ tend to become almost identical (Yoffe 1970, 1972; McIntyre *et al.* 1970; Ohr 1978). In the case of copper, which is fairly anisotropic evidence for this tendency is found on our experimental images of edge-on Frank loops.

6. Discussion and conclusions

The results in this paper indicate that the method of constructing displacement fields of dislocation loops of edge, shear and mixed character, and of stacking-fault tetrahedra by the angular dislocation method of Yoffe (1960) can be usefully employed to produce computer-simulated electron microscope images of these defects. The analytic nature of the displacement fields ensures speed of computation. The displacement field of the stacking-fault tetrahedron has enabled computer-simulated images of this defect to be produced for the first time. This paper clearly demonstrates that a great deal of information about small dislocation loops and stacking-fault tetrahedra (e.g. Burgers vectors, habit planes, vacancy or interstitial character, sizes, etc.) may be obtained with the use of dynamical two-beam conditions in the electron microscope, if micrographs so obtained are studied in conjunction with a computer simulation system. On one hand agreement with experimental images has enabled the identification of defect types, and the technique is of use in determining optimum conditions for, say, loop counting experiments in radiation-damage studies (see, for example, Stathopoulos 1977). On the other hand contrast in untested experimental conditions can be predicted.

The image simulation system described here may also be used to aid the interpretation of 'weak-beam' images (Cockayne *et al.* 1969). One drawback of the 'weak-beam' technique for a study of small defect clusters is a more rapid variation of the contrast with the depth of the defect (due to the smaller effective extinction length) which may lead to greater difficulties in characterising the defect from its image. Detailed experimental studies at Oxford (A. Y. Stathopoulos, to be published) indicate that for heavy-ion irradiation damage which lies close to the foil surface, about 20 % of the small defect clusters visible under strong-beam conditions are out of contrast (despite the use of a highly convergent beam). For larger defects (of sizes greater than 10–15 nm), Jenkins (1974) has shown that the smaller image width of dislocations under weak-beam conditions may give detailed information about the geometries of defects (e.g. mode of dissociation). Further applications of the simulation system with angular dislocation models of the defects could facilitate the understanding of these observations.

The authors wish to thank Professor Sir Peter Hirsch, F.R.S., for the provision of laboratory facilities and for many useful discussions. Two of us wish to acknowledge financial support from

the following sources: the Atomic Energy Research Establishment, Harwell (D. K. S. and A. Y. S.) and the Central Electricity Generating Board (D. K. S.).

Appendix. Determinants of forms of black–white lobes

Hausserman *et al.* (1972) have drawn attention to the great varieties of forms of the black–white lobes of the contrast figure of small dislocation loops and have suggested that they are determined by the relative orientations of $\boldsymbol{b}$, $\boldsymbol{n}$ and $\boldsymbol{g}$. The analysis given below identifies the physical reasons for the forms of the distribution of the lobes, and in the case of the edge-on loop with its Burgers vector parallel to the image plane, gives a criterion for the number of lobes expected for given directions of $\boldsymbol{b}$, $\boldsymbol{n}$ and $\boldsymbol{g}$.

The lobes in the contrast figures are determined by the long-range parts of the strain field. An analysis of their configuration can therefore be made using the strain fields generated by the infinitesimal loop model (Eshelby 1957). Consider the system of axes x_1, x_2 x_3, where the x_1 and x_2 axes are parallel to the image plane and the x_3 axis is antiparallel to the electron beam direction. Now choose the x_1 axis to be in the direction of $\boldsymbol{g}$. Then from Eshelby's (1957) formula, the x_i component of the displacement field at a point $P(x_1, x_2, x_3)$ due to an infinitesimal dislocation loop centred at the origin is,

$$u_i = \frac{-A}{8\pi(1-\nu)\,r^2} \sum_j \sum_k b_j\, n_k\, g_{ijk}, \tag{A 1}$$

where ν is Poisson's ratio, A is the area of the loop, r is the distance OP, b_j, n_k are the components of $\boldsymbol{b}$ and $\boldsymbol{n}$ and

$$g_{ijk} = (1-2\nu)\left\{\delta_{ij}\frac{x_k}{r} + \delta_{ik}\frac{x_j}{r} - \delta_{jk}\frac{x_i}{r}\right\} + \frac{3x_i\,x_j\,x_k}{r^3}.$$

(x_1, x_2, x_3 are the components of $\boldsymbol{r}$. The sign of the right hand side of equation (A 1) is chosen to make it consistent with the FS/RH rule, and is different from that in Eshelby's (1957) paper where an opposite convention is employed.) In the case of $\boldsymbol{b}$ and $\boldsymbol{n}$ lying in the x_1–x_2 plane, if the displacement field is considered as a function of x_3, it is expected to be a maximum in the plane $x_3 = 0$. In fact an overall view of the sense of curvature of the lattice planes in any particular column parallel to the x_3 axis may be obtained from the direction of the displacement at $x_3 = 0$ since it is known that the displacements tend to zero for $x_3 \to \pm\infty$. In the case of $\boldsymbol{g}$ parallel to the x_1 axis, the only component of the displacement field contributing to the image contrast is u_1. The sign of the lobe (i.e. whether black or white) depends on the sense of curvature of the lattice planes in a column parallel to the x_3 axis passing through the lobe. The above arguments show that this is determined by the sign of u_1 in the plane $x_3 = 0$. The boundaries between the lobes are determined by the condition $u_1 = 0$ for $x_3 = 0$. Substituting these values into equation (A 1) leads to the following equation,

$$\begin{aligned}\eta^3[(1-2\nu)\,(b_1 n_2 + b_2 n_1)] + \eta^2[(1-2\nu)\,(b_1 n_1 - b_2 n_2) + 3b_2 n_2] \\ + \eta[\{3+(1-2\nu)\}\,(b_1 n_2 + b_2 n_1)] + (1-2\nu)\,(b_1 n_1 - b_2 n_2) + 3b_1 n_1 = 0,\end{aligned} \tag{A 2}$$

where $\eta = x_2/x_1$. This cubic equation η has in general either one or three real roots. The solutions of this equation therefore determines either one or three straight lines in the image plane, passing through the projected centre of the loop, which form the boundaries of the black and the white lobes. Hence the former case gives rise to one black and one white lobe (i.e. the 'normal'

black–white image) and the latter case six alternate black and white lobes (i.e. the 'butterfly' image).

Comparisons of the solutions of equation (A 2) (found by standard analytic methods) with the computer-simulated images of this paper showed that not only the image type but also the positions of the boundaries of the lobes were accurately predicted. If equation (A 2) is written in the form

$$\eta^3 + b\eta^2 + c\eta + d = 0, \tag{A 3}$$

the number of lobes expected is determined by the sign of the quantity,

$$\Delta = \tfrac{1}{27}c^3 + \tfrac{1}{4}d^2 - \tfrac{1}{6}dbc + \tfrac{1}{27}b^3 d - \tfrac{1}{108}c^2 b^2 \tag{A 4}$$

a positive sign corresponding to the 'normal' black–white image and a negative sign to the 'butterfly' image.

References

Bullough, R., Maher, D. M. & Perrin, R. C. 1971 *Phys. Stat. Sol.* B **43**, 689.

Carter, C. B. & Ray, I. L. F. 1977 *Phil. Mag.* **35**, 189.

Chik, K.-P. 1966 *Phys. Stat. Sol.* **16**, 685.

Cockayne, D. J. H., Ray, I. L. F. & Whelan, M. J. 1969 *Phil. Mag.* **20**, 1265.

Cockayne, D. J. H., Jenkins, M. L. & Ray, I. L. F. 1971 *Phil. Mag.* **24**, 1383.

English, C. A., Eyre, B. L., Holmes, S. M. and Perrin, R. C., 1978 *Electron Diffraction* 1927–1977 (ed. P. J. Dobson *et al.*). *Proc. Int. Conf., London.* 1977. Bristol: *Inst. Phys. Conf. Ser.*, no. 41, p. 381.

Essmann, U. & Wilkens, M. 1964 *Phys. Stat. Sol.* **4**, K 53.

Eshelby, J. D. 1957 *Proc. R. Soc. Lond.* A **241**, 376.

Eyre, B. L. 1972 *Defects in refractory metals* (ed. R. de Batist), Proc. Discussion Meeting, Mol 1971, Mol: S.C.K./C.E.N., p. 311.

Eyre, B. L. & Bullough, R. 1965 *Phil. Mag.* **11**, 31.

Eyre, B. L., Maher, D. M. & Perrin, R. C. 1977*a*, *b*, *J. Phys.* F **7**, 1359, 1371.

Gill, S. 1951 *Proc. Camb. Phil. Soc.* **47**, 96.

Haussermann, F., Ruhle, M. & Wilkens, M. 1972 *Phys. Stat. Sol.* B **50**, 445.

Head, A. K., Humble, P., Clarebrough, L. M., Morton, A. J. & Forwood, C. T. 1973 *Defects in Crystalline Solids*, vol. 7 (ed. S. Amelinckx *et al.*), p. 38. Amsterdam: North-Holland.

Hirsch, P. B. 1978 *Electron diffraction* 1927–1977 (ed P. J. Dobson *et al.*) *Proc. Int. Conf.*, London, 1977. Bristol: *Inst. Phys. Conf. Ser.* no. 41, p. 335.

Hirsch, P. B., Howie, A., Nicholson, R. B., Pashley, D. W. & Whelan, M. J. 1965 *Electron microscopy of thin crystals*, p. 205. London: Butterworths.

Hirsch, P. B., Howie, A. & Whelan, M. J. 1960 *Phil. Trans. R. Soc. Lond.* A **252**, 499.

Holmes, S. M., Eyre, B. L. and Perrin, R. C. 1976 *Electron microscopy* 1976 (ed. D. G. Brandon). *Proc. 6th Eur. Reg. Cong.* Jerusalem, vol. I, p. 279. Jerusalem: TAL International.

Howie, A. & Whelan, M. J. 1961 *Proc. R. Soc. Lond.* A **263**, 217.

Jenkins, M. L. 1974 *Phil. Mag.* **29**, 813.

Katerbau, K.-H. 1976 *Phys. Stat. Sol.* A **38**, 463.

Katerbau, K.-H. 1978 *Electron microscopy* 1978. *Proc. 9th Int. Cong. Electron Microscopy*, Toronto 1978 (ed. J. M. Sturgess), vol. I. p. 184. Toronto: Microscopical Society of Canada.

Maher, D. M., Perrin, R. C. & Bullough, R. 1971 *Phys. Stat. Sol.* B **43**, 707.

McIntyre, K. G. Brown, L. M. & Eades, J. A. 1970 *Phil. Mag.* **21**, 853.

Ohr, S. M. 1973 *Defects and defect clusters in B.C.C. metals and their alloys* (ed. R. J. Arsenault), p. 62. *Proc. Int Conf.*, 1973. Gaithersburg: National Bureau of Standards.

Ohr, S. M. 1976 *Phys. Stat. Sol.* A **38**, 553.

Ohr, S. M. 1978 *Electron microscopy* 1978. *Proc. 9th Int. Cong. Electron Microscopy*, Toronto, 1978 (ed. J. M. Sturgess). vol. I, p. 326. Toronto: Microscopical Society of Canada.

Radi, G. 1970 *Acta crystallogr.* A **26**, 41.

Ruhle, M. 1969 *Radiation damage in reactor materials. Proc. Symp.*, Vienna, 1969, vol. I, p. 113. Vienna: International Atomic Energy Agency.

Ruhle, M., Wilkens, M. and Essmann, U. 1965 *Phys. Stat. Sol.* **11**, 819.

Saldin, D. K. and Whelan, M. J. 1975 *Developments in electron microscopy and analysis* (ed. J. Venables), p. 393 Proc. EMAG 75, Bristol 1975. London: Academic Press.

Saldin, D. K., Stathopoulos, A. Y. & Whelan, M. J 1978*a* *Electron diffraction* 1927–1977 (ed. P. J. Dobson *et al.*). *Proc. Int. Conf.*, London, 1977. Bristol: *Inst Phys. Conf. Ser.* no. 41, p. 350.

Saldin, D. K., Whelan, M. J. & Rossouw, C. J. 1978*b* *Electron diffraction* 1927–1977 (ed. P. J. Dobson *et al.*). *Proc. Int. Conf.*, London, 1977. Bristol: *Inst. Phys. Cong. Ser.* no. 41, p. 50.

Silcox, J. & Hirsch, P. B. 1959 *Phil. Mag.* **4**, 72.

Smith, G. H. & Burge, R. E. 1962 *Acta crystallogr.* **15**, 182.

Stathopoulos, A. Y. 1977 D. Phil. thesis, University of Oxford.

Stobbs, W. M. & Sworn, C. H. 1971 *Phil. Mag.* **24**, 1365.

Thompson, N. 1953 *Proc. Phys. Soc.*, B **66**, 481.

Wilkens, M. 1970*a* *Modern diffraction and imaging techniques in materials science* (ed. Amelinckx *et al.*), p. 233. *Proc. N.A.T.O. Summer Course, Antwerp*, 1969. Amsterdam: North-Holland.

Wilkens, M. 1970*b* *Vacancies and interstitials in metals* (ed. A. Seeger *et al.*), p. 485. *Proc. Int. Conf., Julich*, 1968. Amsterdam: North-Holland.

Wilson, M. M. 1969 *Radiat. Effects* **1**, 207.

Wilson, M. M. 1971 *Phil. Mag.* **24**, 1023.

Yoffe, E. H. 1960 *Phil. Mag.* **5**, 161.

Yoffe, E. H. 1970 *Phil. Mag.* **21**, 833.

Yoffe, E. H. 1972 *Phil. Mag.* **25**, 935.

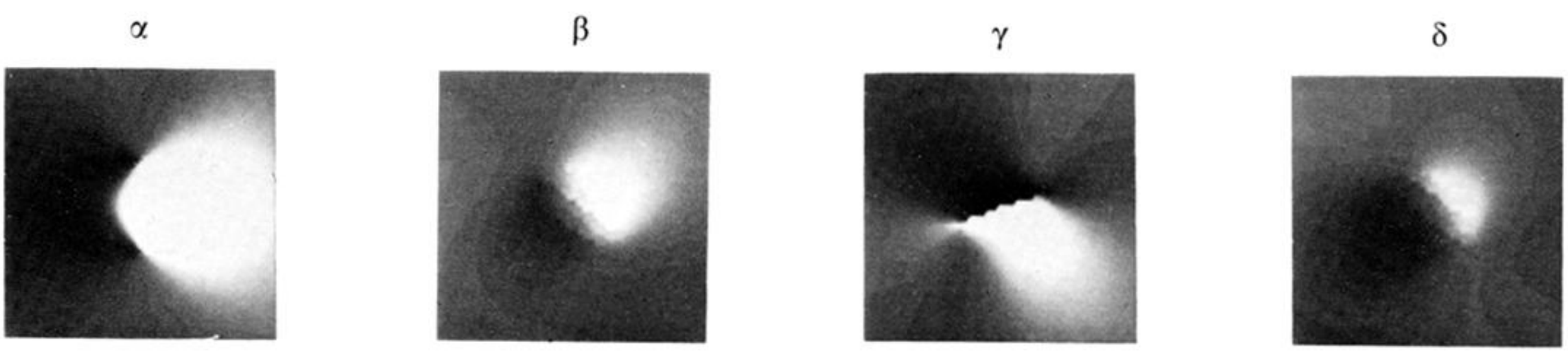

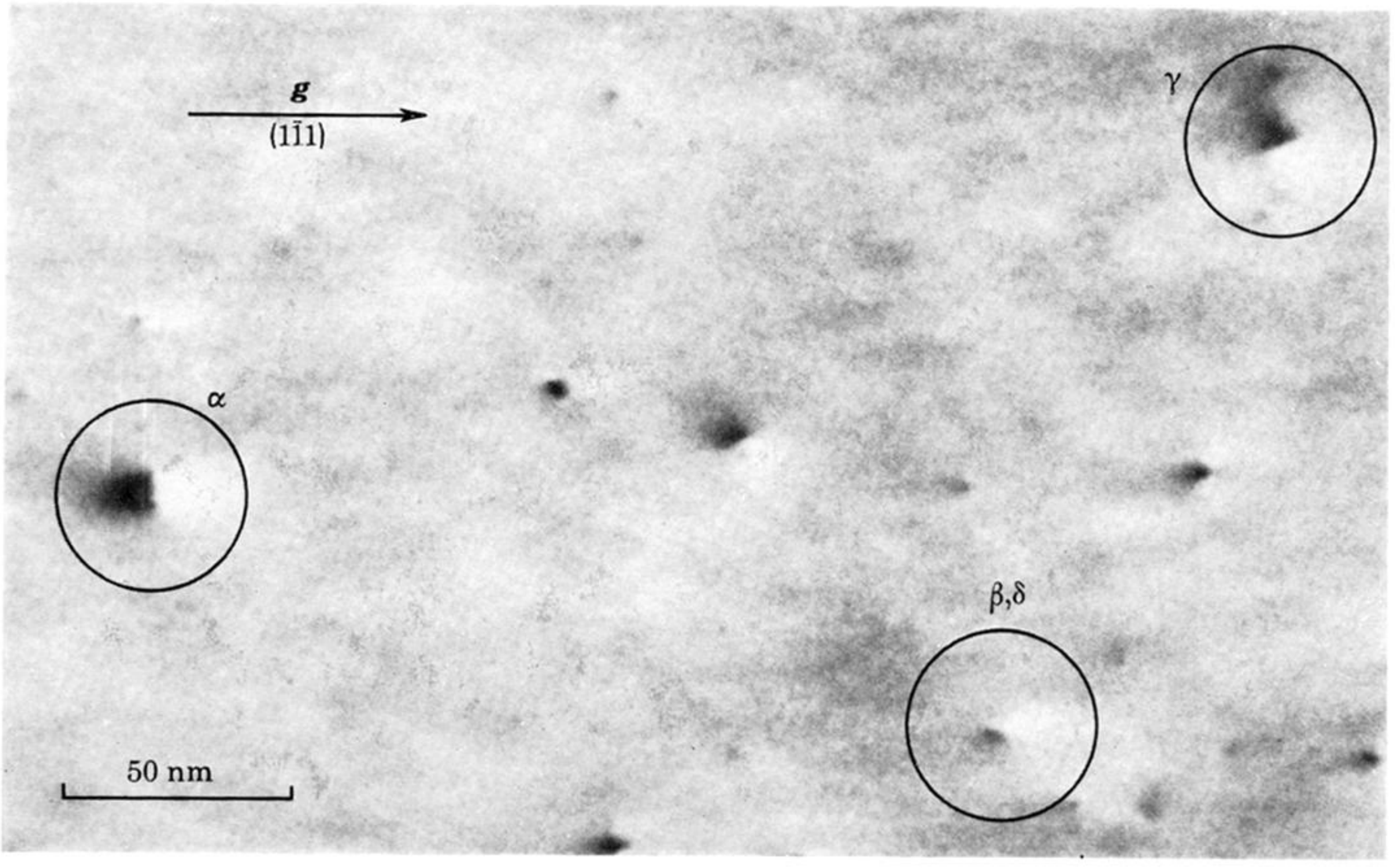

FIGURE 2. For description see opposite.

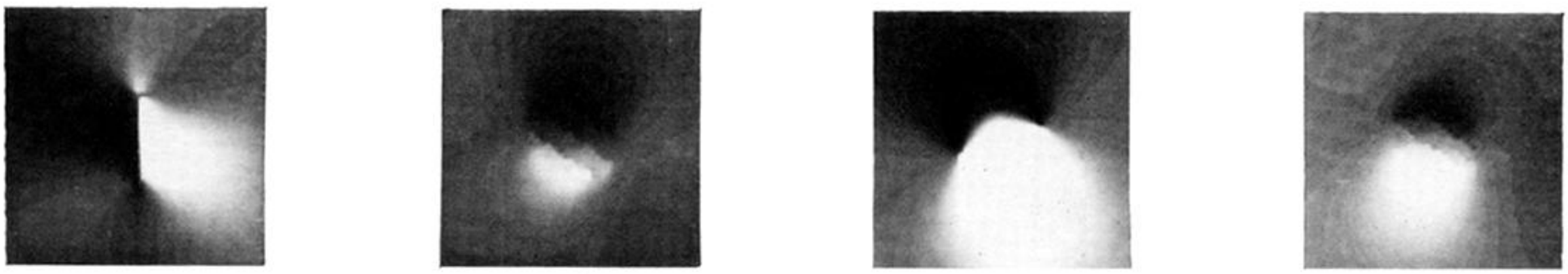

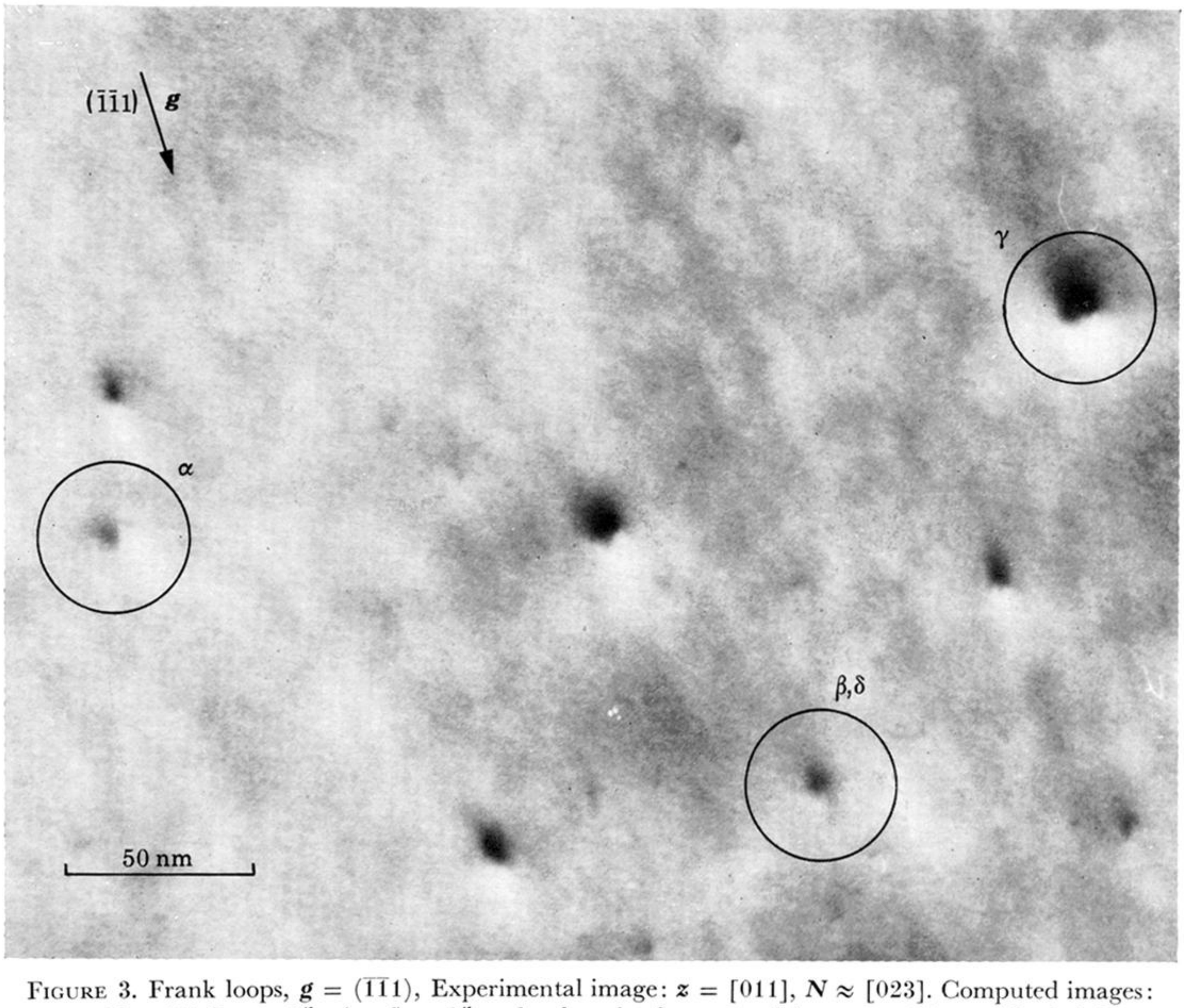

FIGURE 3. Frank loops, $\boldsymbol{g} = (\bar{1}\bar{1}1)$, Experimental image: $\boldsymbol{z} = [011]$, $\boldsymbol{N} \approx [023]$. Computed images: $\boldsymbol{z} = \boldsymbol{N} = [011]$, $t = 2\xi_g$, $(t-d) = \frac{1}{8}\xi_g$; edge length of computed images = 8.1 nm. Dark field.

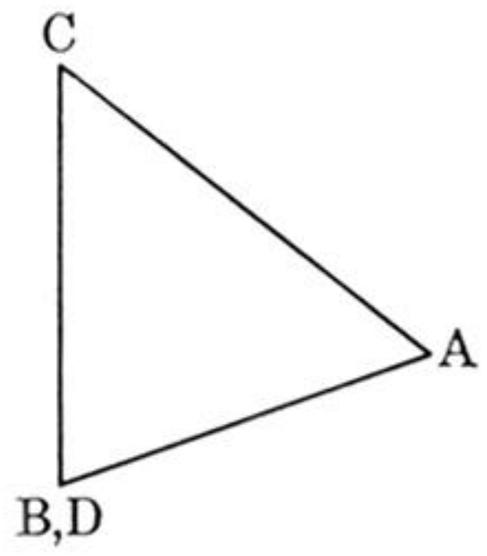

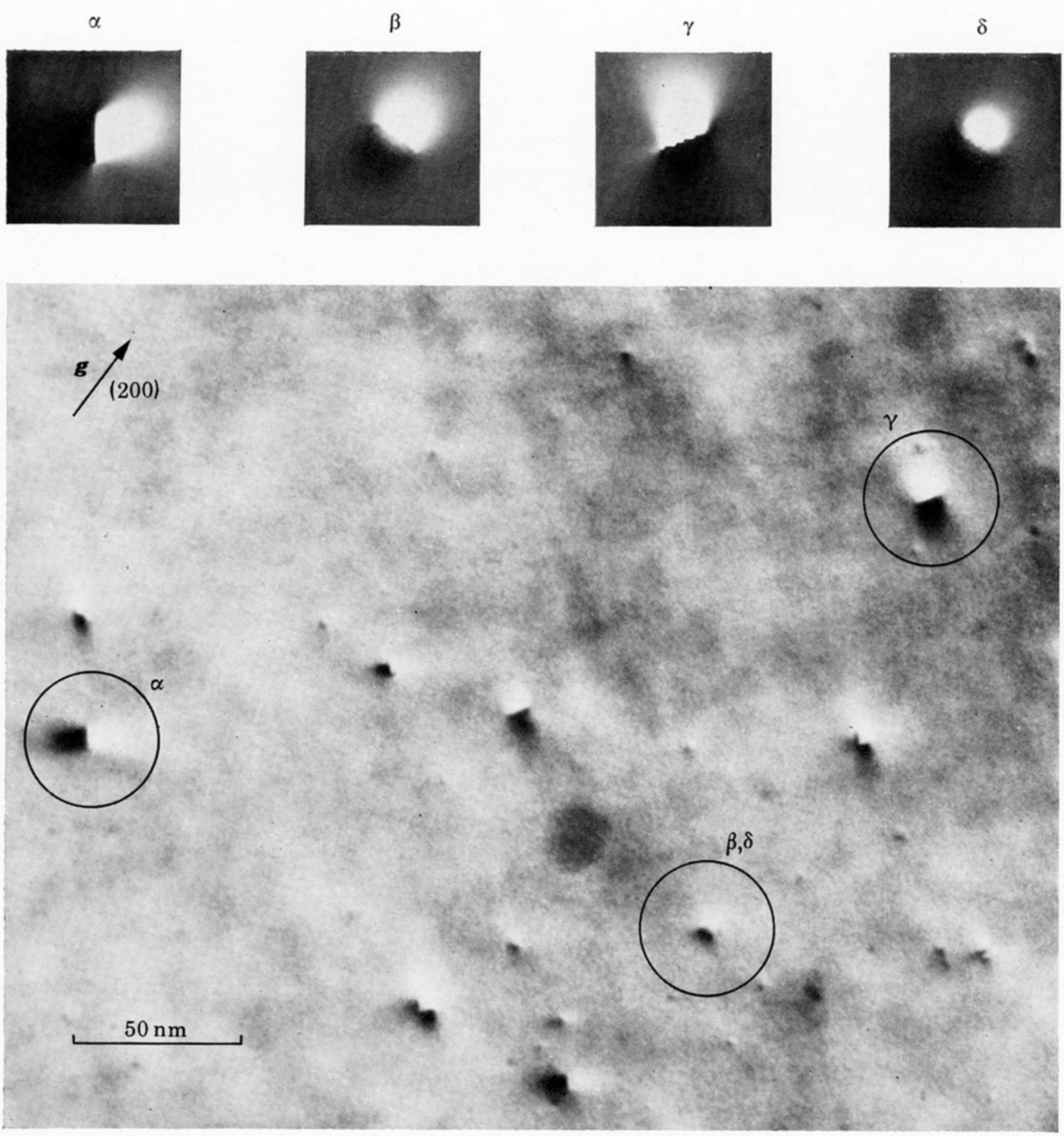

FIGURE 4. Frank loops, $\boldsymbol{g} = (200)$. Experimental image: $\boldsymbol{z} = [011]$, $\boldsymbol{N} \approx [023]$. Computed images: $\boldsymbol{z} = \boldsymbol{N} = [011]$, $t = 2\xi_g$, $(t-d) = \frac{1}{8}\xi_g$; edge length of computed images = 9.4. Dark field.

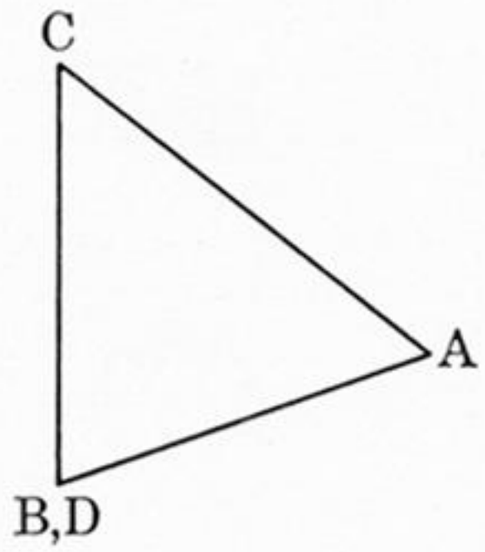

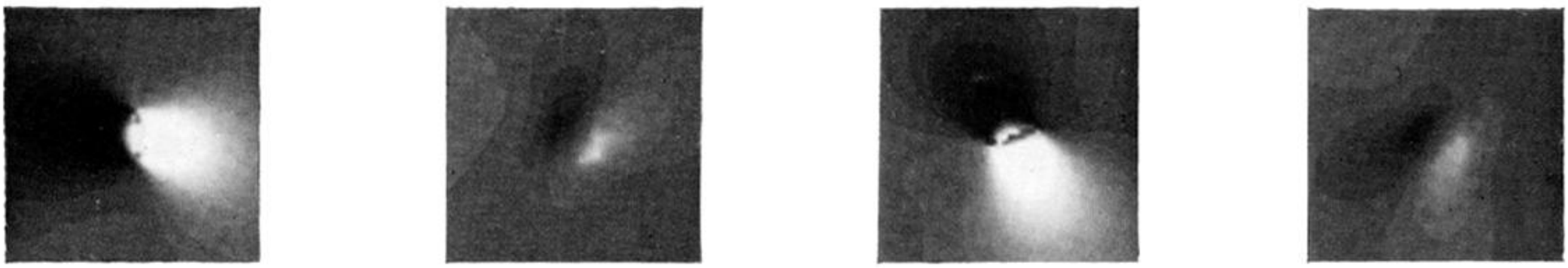

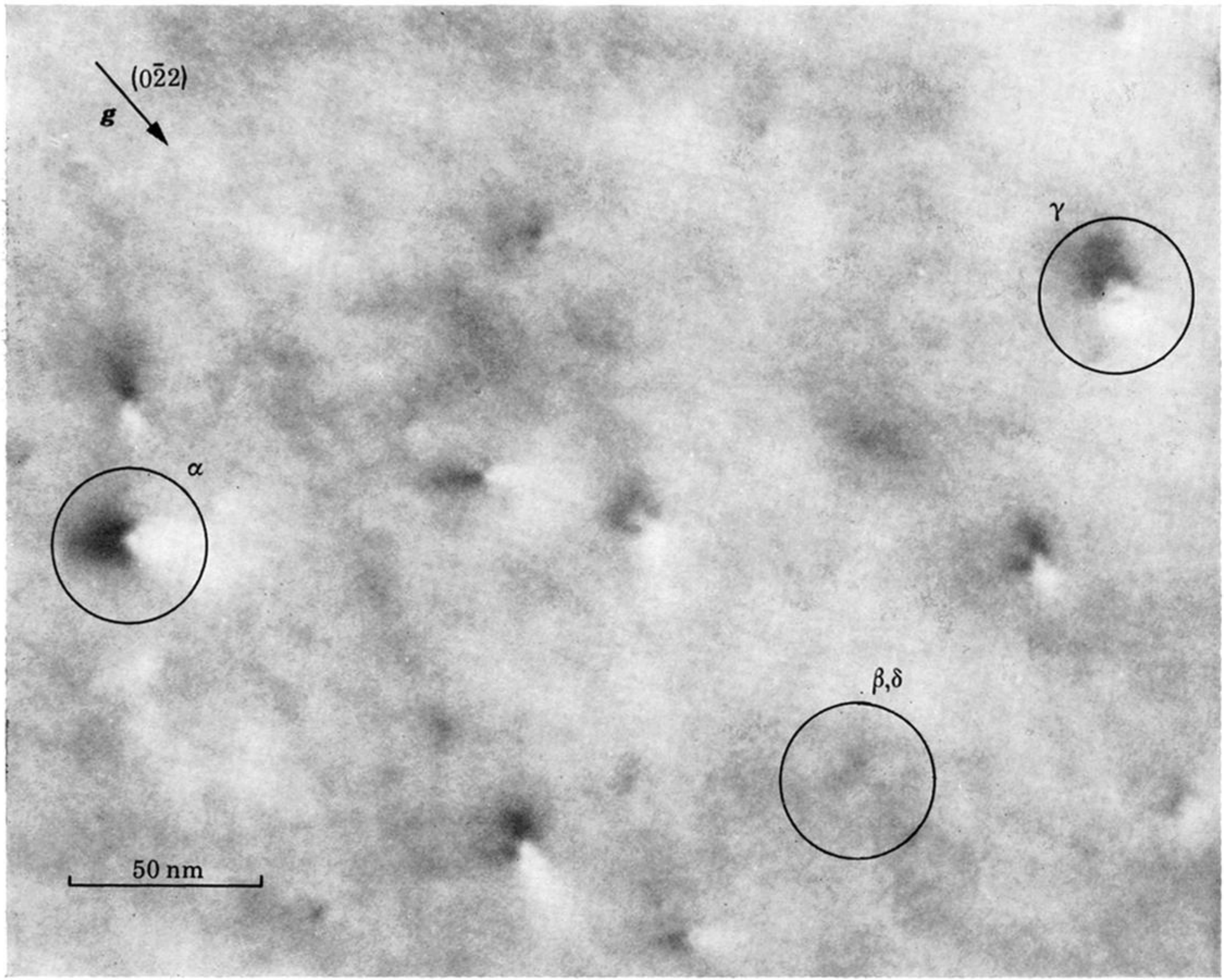

FIGURE 5. For description see opposite.

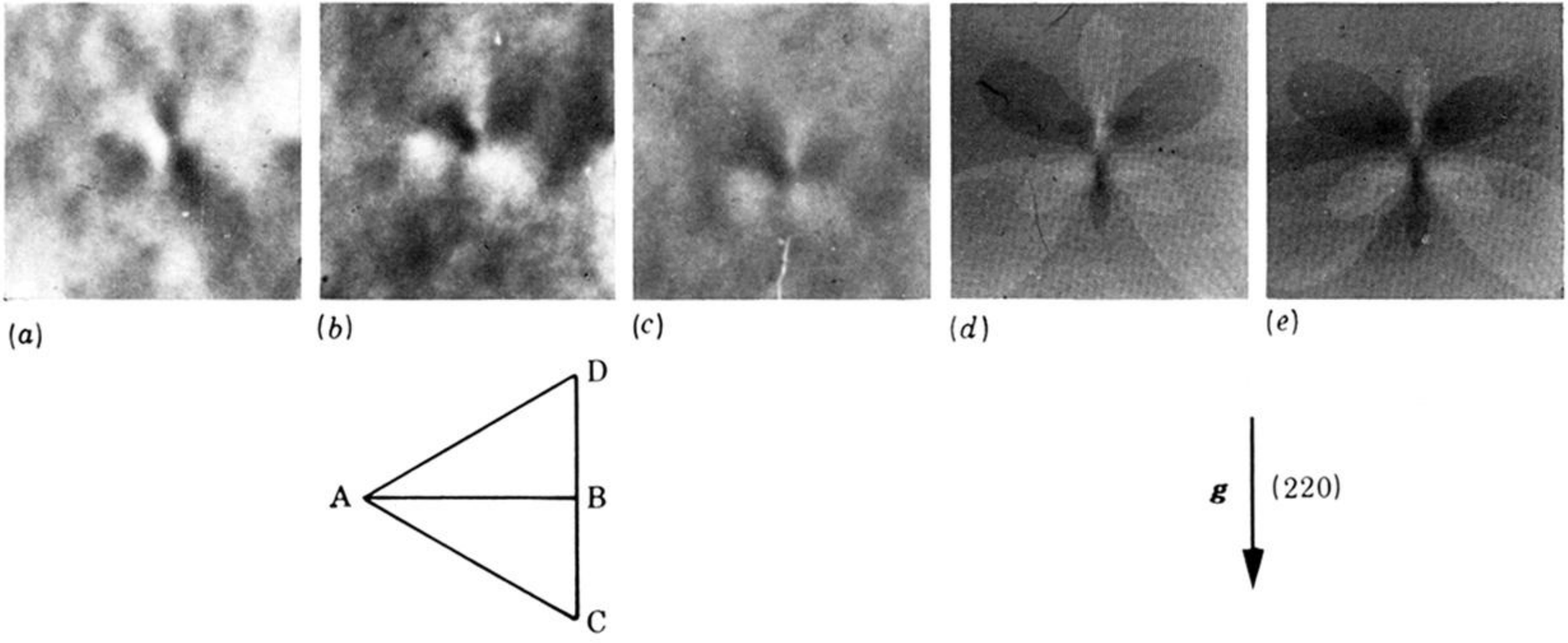

FIGURE 6. Frank loops, butterfly images. Experimental images: (*a*) Dark field $\boldsymbol{g} = (\bar{2}\bar{2}0)$, (*b*) dark field $\boldsymbol{g} = (220)$, (*c*) bright field $\boldsymbol{g} = (\bar{2}\bar{2}0)$. Loop plane α. $\boldsymbol{z} = [\bar{1}12]$, $\boldsymbol{N} \approx [023]$. Computed images: $\boldsymbol{z} = [\bar{1}12]$, $t = 4\xi_g$, $(t-d) = \frac{1}{8}\xi_g$, $\boldsymbol{g} = (220)$, $\boldsymbol{b} = \frac{1}{3}a[\bar{1}1\bar{1}]$, $\boldsymbol{g}\cdot\boldsymbol{b} = 0$; (*d*) $\boldsymbol{N} = [\bar{1}12]$, (*e*) $\boldsymbol{N} = [023]$. Edge length of experimental images = 50 nm; edge length of computed images = 14 nm.

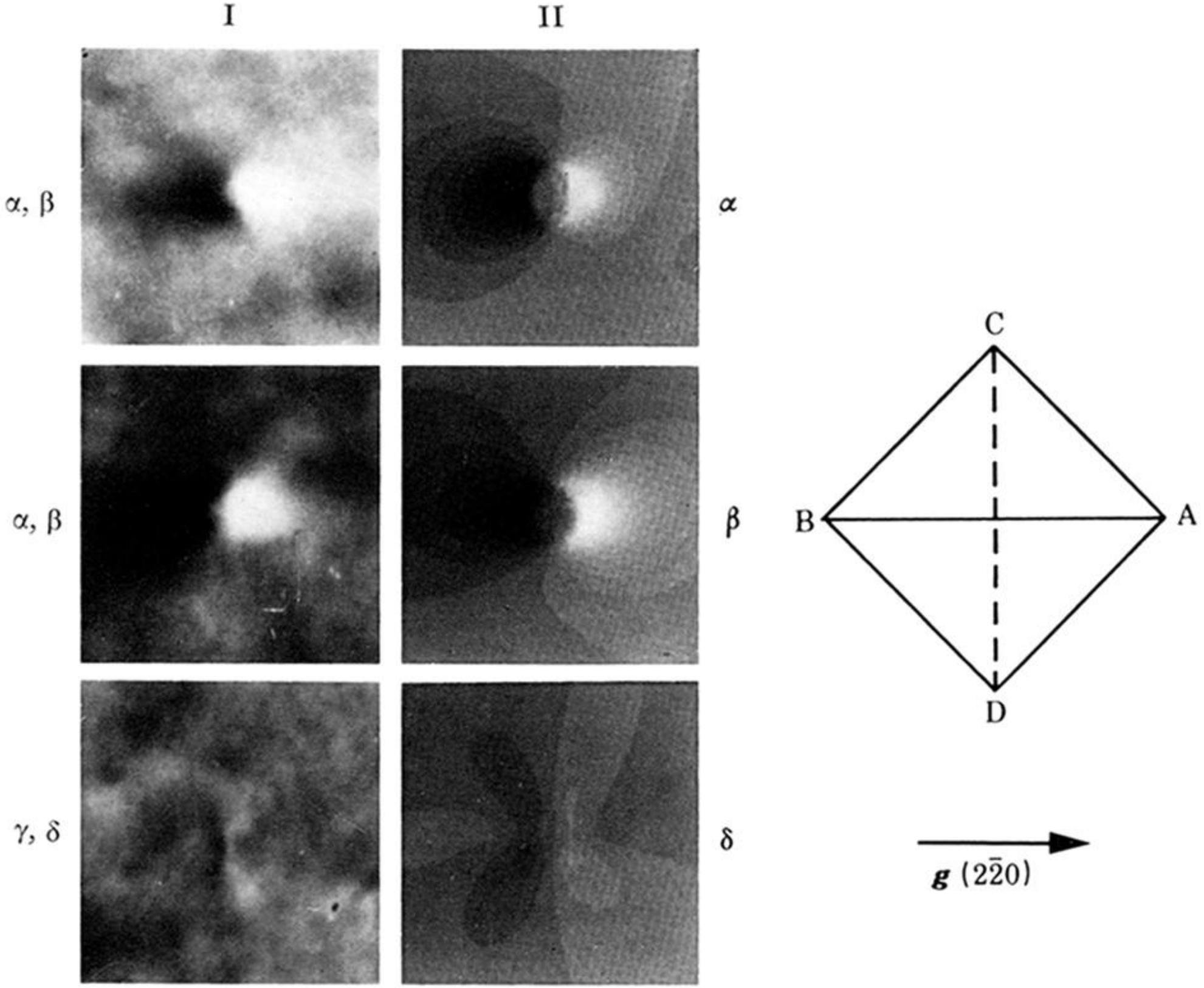

FIGURE 8. Frank loops, images at [001] orientation, $\boldsymbol{g} = (2\bar{2}0)$. Column I: Experimental images: $\boldsymbol{z} = [001]$, $\boldsymbol{N} \approx [023]$. Column II: Computed images: $\boldsymbol{z} = [001]$, $\boldsymbol{N} = [023]$, $t = 4\xi_g$, $(t-d) = \frac{1}{8}\xi_g$. Edge length of experimental images = 50 nm; edge length of computed images = 14 nm. Dark field.

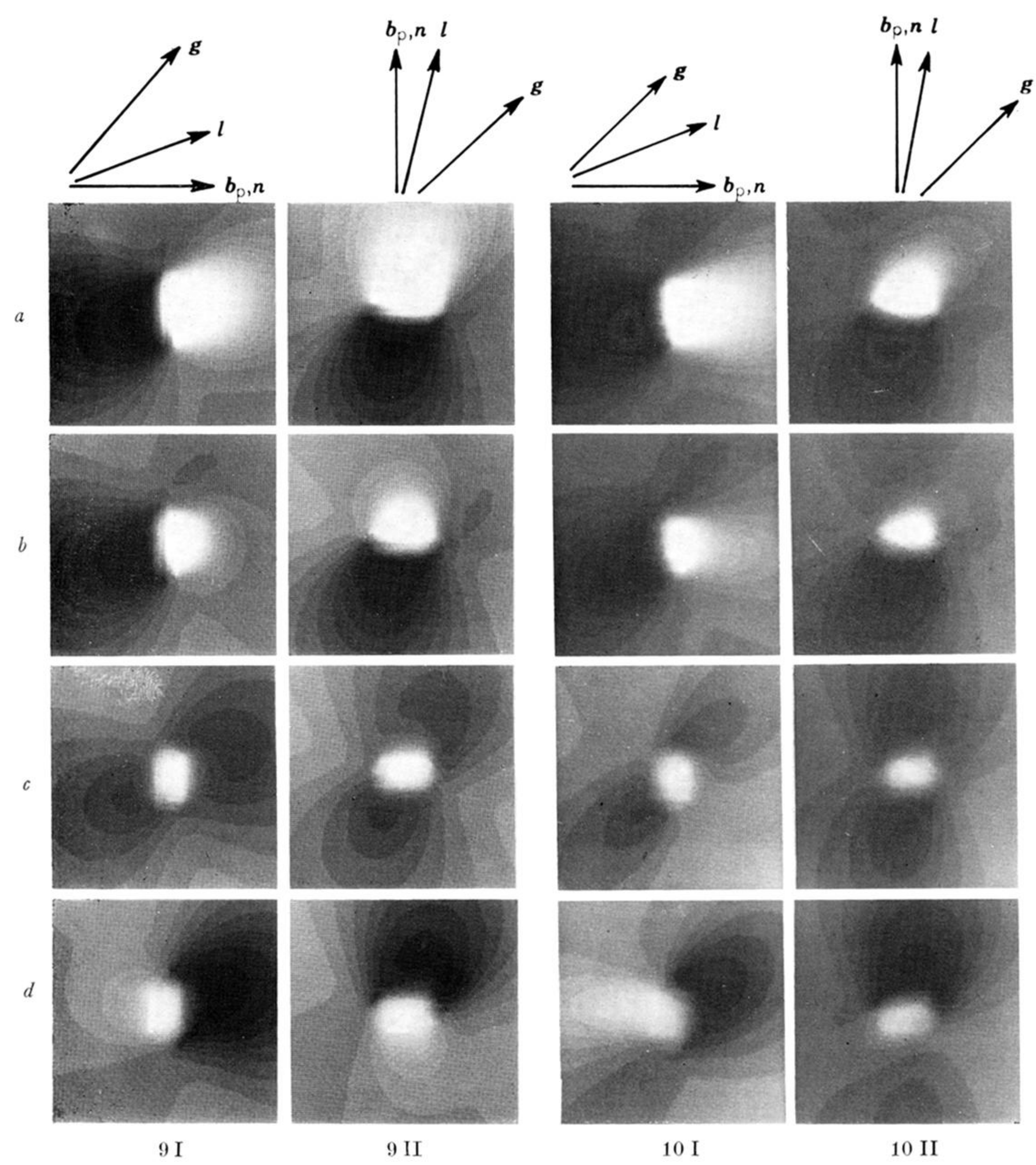

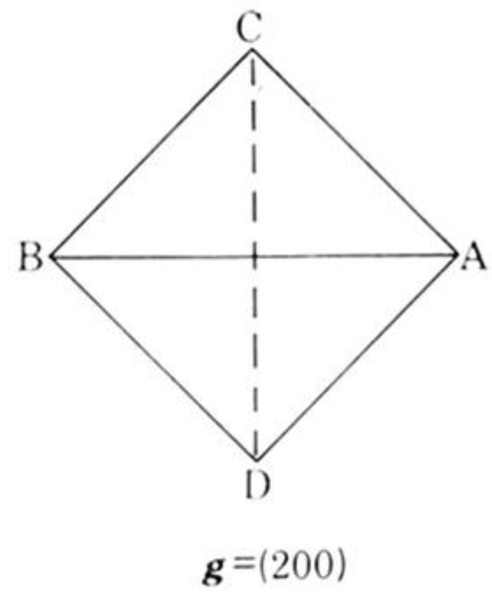

FIGURE 9. Frank loops, dependence of contrast on depth, $\boldsymbol{g} = (200)$. Computed images: $\boldsymbol{z} = \boldsymbol{N} = [001]$, $t = 4\xi_g$; (*a*) $(t-d) = \frac{1}{8}\xi_g$; (*b*) $(t-d) = \frac{3}{16}\xi_g$; (*c*) $(t-d) = \frac{1}{4}\xi_g$; (*d*) $(t-d) = \frac{5}{16}\xi_g$. Column I: loop plane α; column II: loop plane δ. Edge length of images = 8.2 nm. Dark field.

FIGURE 10. Frank loops, dependence of contrast on depth. $\boldsymbol{N} = [023]$. All other parameters same as for figure 9.

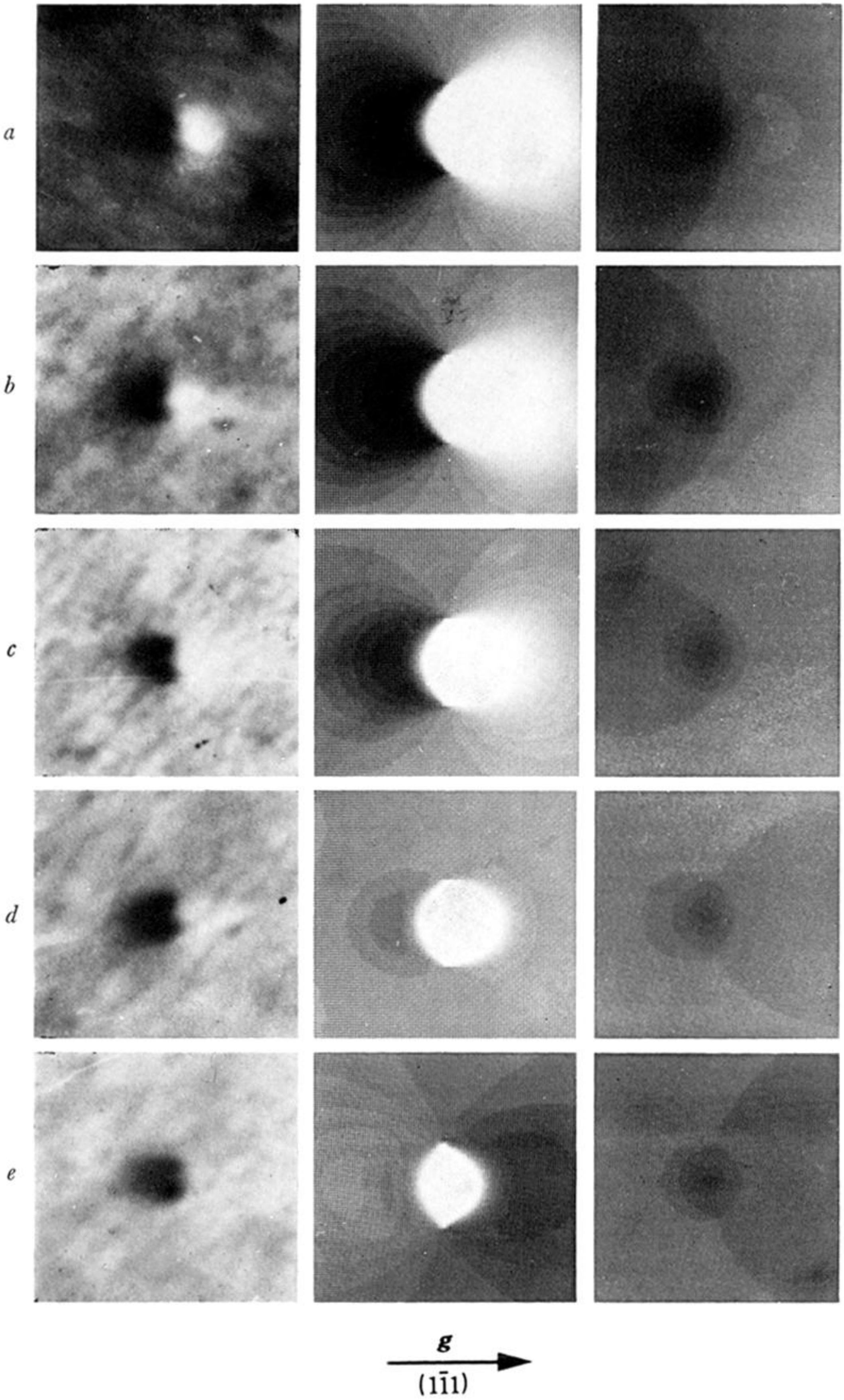

FIGURE 11. For description see opposite.

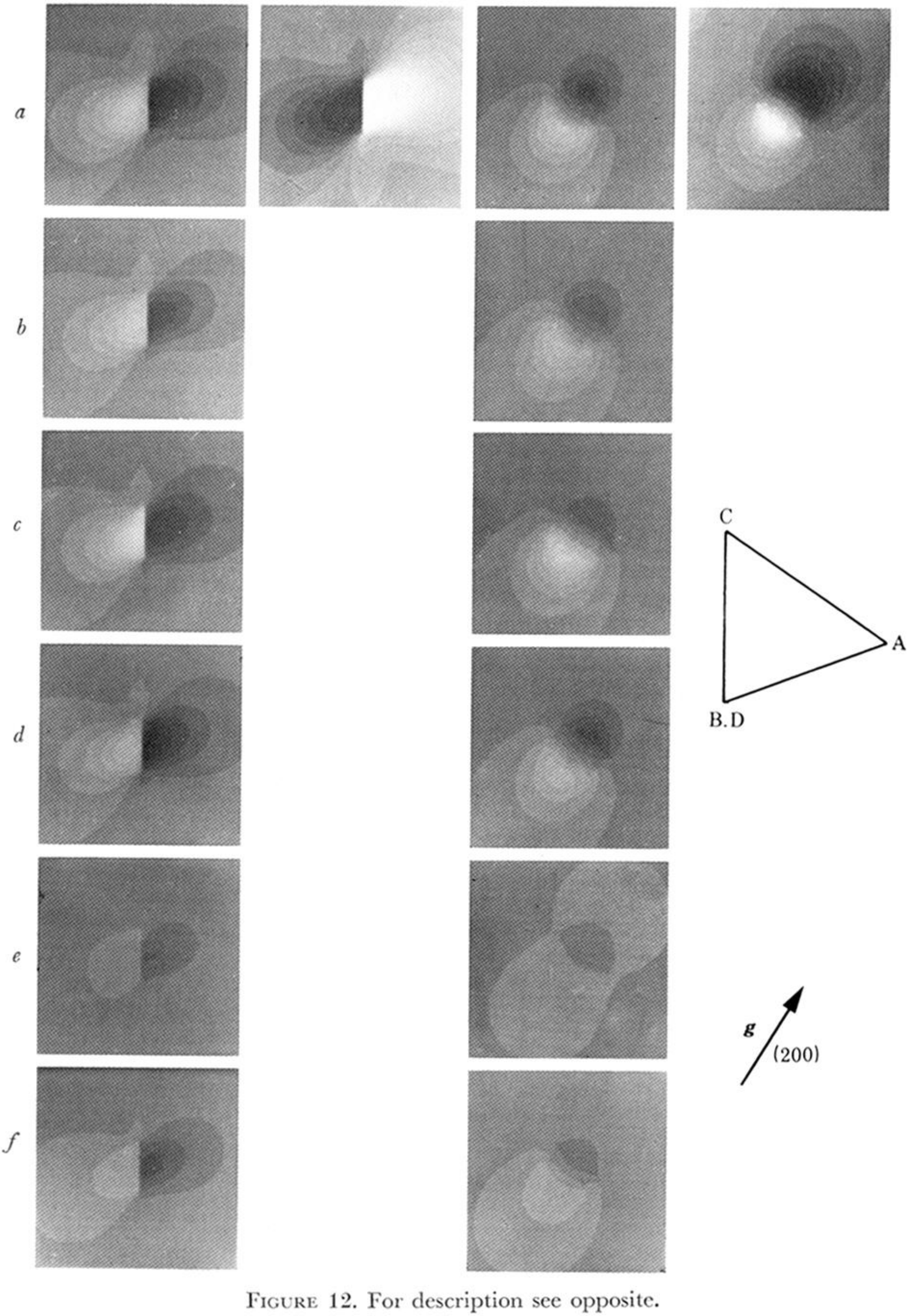

FIGURE 12. For description see opposite.

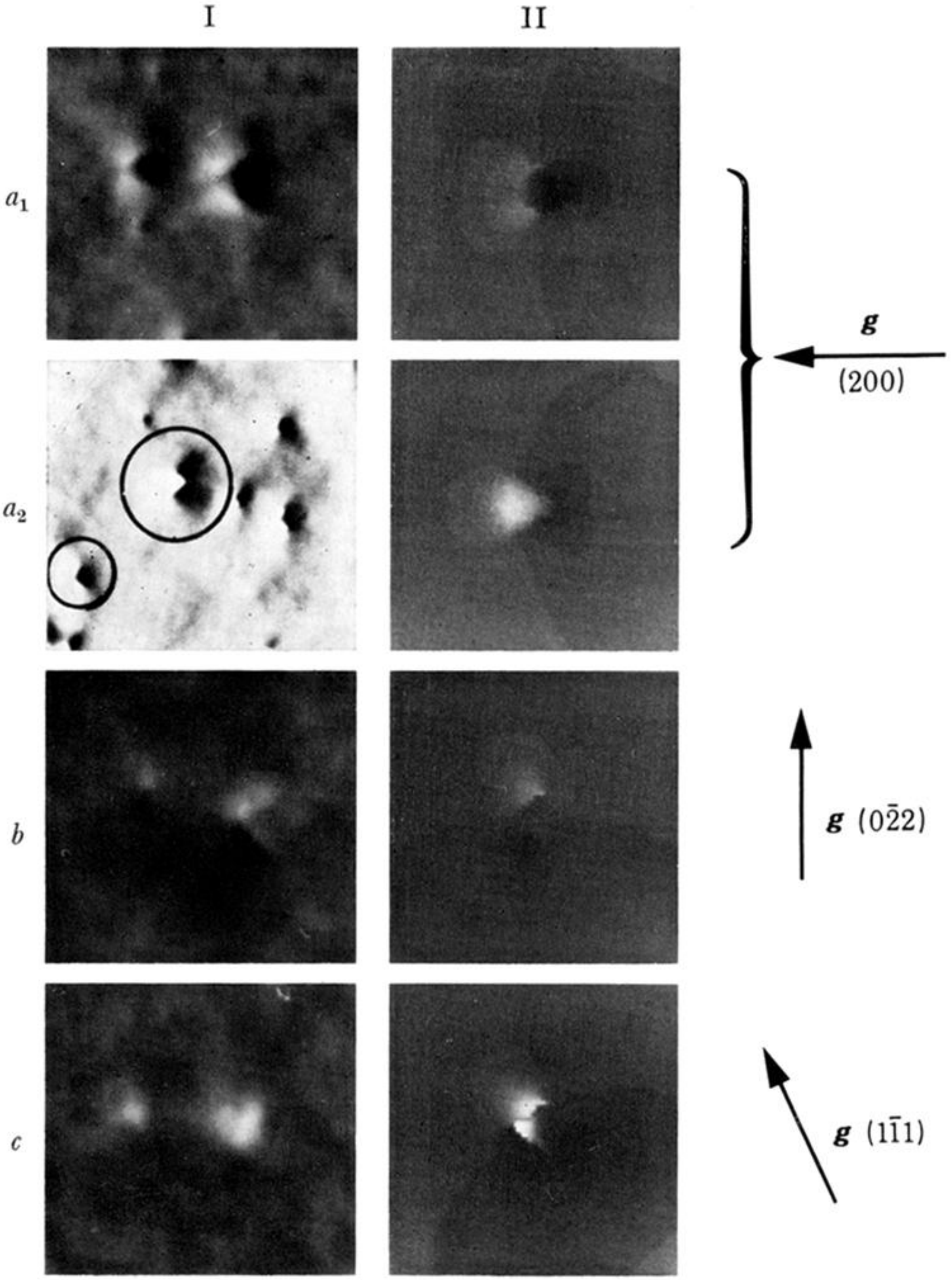

FIGURE 13. Stacking-fault tetrahedra, $\boldsymbol{z} = [011]$. (a_1) Orientation 1, $\boldsymbol{g} = (200)$; (a_2) orientation 2, $\boldsymbol{g} = (200)$; (b) orientation 1, $\boldsymbol{g} = (0\bar{2}2)$; ($c$) orientation 1, $\boldsymbol{g} = (1\bar{1}1)$. Column I : Experimental images: $\boldsymbol{N} \approx [023]$. Column II: Computed images: $\boldsymbol{N} = [023]$, $t = 4\xi_g$, $(t-d) = \frac{1}{8}\xi_g$. Edge length of experimental images = 114 nm, edge length of computed images = 14 nm. Dark field.

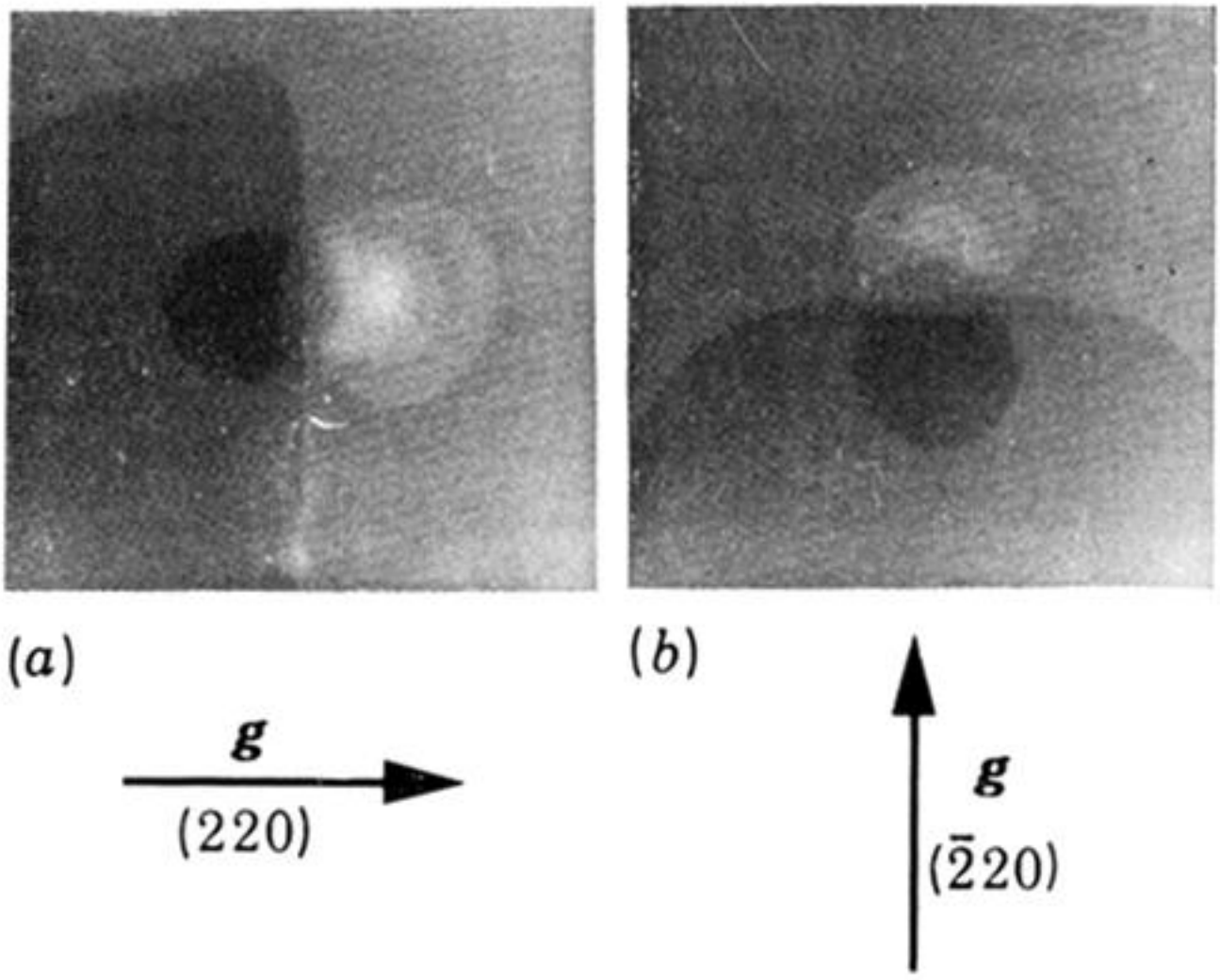

FIGURE 14. Stacking-fault tetrahedron $\boldsymbol{z} = [001]$. Orientation 2. Computed images: $\boldsymbol{N} = [023]$, $t = 4\xi_g$, $(t-d) = \frac{1}{8}\xi_g$. (*a*) $\boldsymbol{g} = (220)$, (*b*) $\boldsymbol{g} = (2\bar{2}0)$. Edge length of images = 14 nm. Dark field.

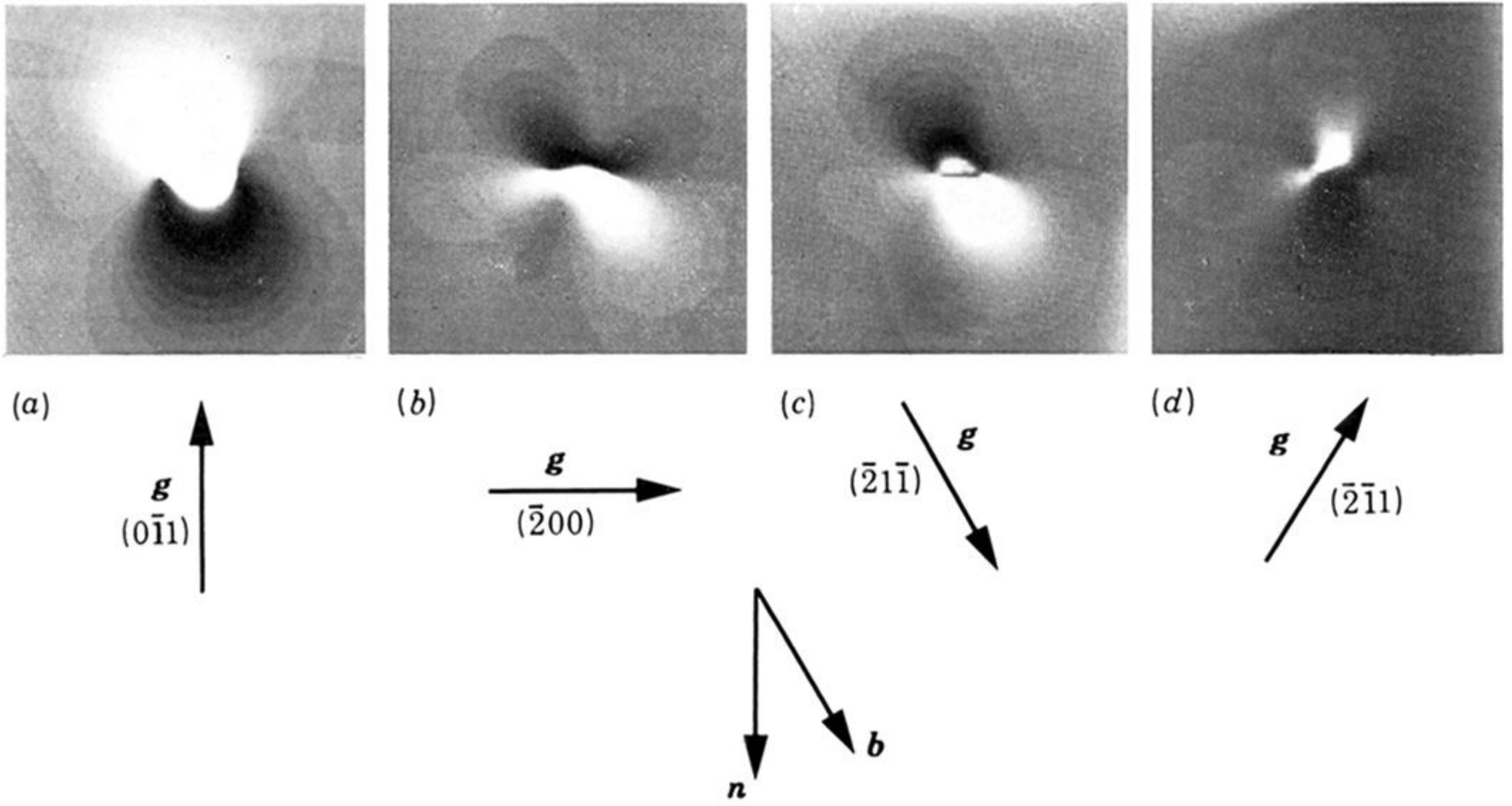

FIGURE 15. Non-edge loops in molybdenum. Computed images: $\boldsymbol{b} = (a/2)\,[\bar{1}1\bar{1}]$, $\boldsymbol{n} = [01\bar{1}]$, $t = 2\xi_g$, $(t-d) = \frac{1}{8}\xi_g$. (*a*) $\boldsymbol{z} = \boldsymbol{N} = [\bar{1}55]$, $\boldsymbol{g} = (0\bar{1}1)$; (*b*) $\boldsymbol{z} = \boldsymbol{N} = [023]$, $\boldsymbol{g} = (\bar{2}00)$; (*c*) $\boldsymbol{z} = \boldsymbol{N} = [\bar{1}35]$, $\boldsymbol{g} = (\bar{2}1\bar{1})$; (*d*) $\boldsymbol{z} = \boldsymbol{N} = [\bar{1}53]$, $\boldsymbol{g} = (\bar{2}\bar{1}1)$. Edge length of images: (*a*) 20.8 nm; (*b*) 29.5 nm; (*c*), (*d*) 36.8 nm. Dark field.